ARMY RESEARCH LABORATORY

Launch Survivability Analysis of On-board Components of the Extended Area Protection and Survivability (EAPS) Projectile System

by Michael M. Chen

ARL-TR-4484 **June 2008**

NOTICES

Disclaimers

The findings in this report are not to be construed as an official Department of the Army position unless so designated by other authorized documents.

Citation of manufacturer's or trade names does not constitute an official endorsement or approval of the use thereof.

DESTRUCTION NOTICE—Destroy this report when it is no longer needed. Do not return it to the originator.

Army Research Laboratory
Aberdeen Proving Ground, MD 21005-5066

ARL-TR-4484 **June 2008**

Launch Survivability Analysis of On-board Components of the Extended Area Protection and Survivability (EAPS) Projectile System

Michael M. Chen
Weapons and Materials Research Directorate, ARL

REPORT DOCUMENTATION PAGE

Form Approved
OMB No. 0704-0188

1. REPORT DATE *(DD-MM-YYYY)*	2. REPORT TYPE	3. DATES COVERED (From - To)
June 2008	Final	October 2007 to May 2008

4. TITLE AND SUBTITLE

Launch Survivability Analysis of On-board Components of the Extended Area Protection and Survivability (EAPS) Projectile System

5a. CONTRACT NUMBER

5b. GRANT NUMBER

5c. PROGRAM ELEMENT NUMBER

6. AUTHOR(S)

Michael M. Chen (ARL)

5d. PROJECT NUMBER

622618.H80

5e. TASK NUMBER

5f. WORK UNIT NUMBER

7. PERFORMING ORGANIZATION NAME(S) AND ADDRESS(ES)

U.S. Army Research Laboratory
Weapons and Materials Research Directorate
Aberdeen Proving Ground, MD 21005-5066

8. PERFORMING ORGANIZATION REPORT NUMBER

ARL-TR-4484

9. SPONSORING/MONITORING AGENCY NAME(S) AND ADDRESS(ES)

10. SPONSOR/MONITOR'S ACRONYM(S)

11. SPONSOR/MONITOR'S REPORT NUMBER(S)

12. DISTRIBUTION/AVAILABILITY STATEMENT

Approved for public release; distribution is unlimited.

13. SUPPLEMENTARY NOTES

14. ABSTRACT

This report focuses on the ability of on-board electronics generally required for precision projectiles to survive pressure waves that occur in early combustion phase for most propelling charges because of pressure imbalance in the chamber. The modeling of pressure waves was achieved by a deterministic transient excitation followed by a stochastic approach. The responses of the on-board electronic components were found to be significant when pressure waves were taken into account.

15. SUBJECT TERMS

electronics; launch dynamics; on-board electronics; survivability analysis

16. SECURITY CLASSIFICATION OF:			17. LIMITATION OF ABSTRACT	18. NUMBER OF PAGES	19a. NAME OF RESPONSIBLE PERSON
a. REPORT	b. ABSTRACT	c. THIS PAGE			Michael M. Chen
Unclassified	Unclassified	Unclassified	SAR	45	19b. TELEPHONE NUMBER (*Include area code*) 410-278-6146

Contents

List of Figures

List of Tables

Acknowledgments

The author would like to thank Dr. William Drysdale, Mr. David Hopkins, and Dr. Brian Powers of the U.S. Army Research Laboratory (ARL) for offering many constructive comments about the research topic. The insight to igniter design issues provided by Dr. Michael Nusca of ARL is greatly appreciated. In addition, the author is grateful to Mr. Michael Minnicino, Mr. T. Gordon Brown, and Mr. Joseph Colburn of ARL for providing projectile geometry, sensor pack model, and base pressure calculation, respectively.

This work was supported in part by a grant of high performance computing time from the U.S. Department of Defense High Performance Computing Modernization program at ARL's Major Shared Resource Center, Aberdeen Proving Ground, Maryland.

INTENTIONALLY LEFT BLANK

1. Introduction

The U.S. Army Research Laboratory (ARL) has been working on a program named Extended Area Protection and Survivability (EAPS) projectile system, the objective of which is to develop guided ammunition technologies to defend the battle space against a variety of presented aerial targets. In general, supporting technologies, including interceptor, sensor, and fire control, which can enable stationary and mobile 360-degree hemispherical extended area protection from direct and indirect fires, are intended to be demonstrated through this program. Among the technologies, reliable and survivable guidance, navigation, and control devices, which are expected to function after they exit a gun barrel, are critical in order to accomplish the mission. Thus, ensuring that the on-board electronic components can withstand a harsh launch environment is very important.

Over the past decade, low-cost micro-machined inertial measurement sensors have progressively emerged into military applications, such as smart munition guidance and operational test and evaluation (*1*). ARL has conducted studies and experiments related to high-g hardened electronic equipment through several mission programs. Some of the examples are described as follows. An in-bore dynamic analysis was performed by Huang and Newill (*2*) on a smart grenade projectile that had a primary payload of a precision electronics unit composed of two composite boards carrying sensors and processors. The deformation and stress responses of the composite materials were derived. Soencksen (*3*) assessed aerodynamic characteristics of a 120-mm M865 projectile and considered the effect of on-board sensor system configuration. Wilson (*4*) proposed on-board navigation of a ballistic ordnance flight control system, including hardware and software development for smart munitions. In his study, low cost, small size, low power, and high-g survivability were discussed. Peregino and Bukowski (*5*) evaluated a refined surface-mounted Endevco model 7270A accelerometer through numerous experimental tests. Recently, failure assessment of electronic packages through computational modeling and simulations has been increasingly addressed. For instance, Powers and Hopkins (*6*) adopted sub-modeling techniques for the analysis of a representative electronic circuit board subject to projectile launch conditions. Accurate stress results were achieved with proper selection of model parameters. In addition, adhesive failure in electronic packages was modeled and studied by Chew et al. (*7*). Specifically, failure of adhesive joints in microelectronic packages, which was attributable to the effects of softening-rehardening was investigated. This report covers preliminary survivability analysis at the on-board component level. In particular, the issue of pressure wave oscillation during launch is addressed.

A flare-stabilized projectile test bed, which was designed to accommodate a sensor pack in the coned space of the tail, was studied. The sensor pack consisted of a few composite boards that carry sophisticated sensors and processors. The mounted electronic devices are encapsulated with epoxy “potting” material in the container. Because of required high-speed velocity at the muzzle,

the tactical projectile system must resist an immense base pressure from launch. The transient excitation that gives rise to significant pressure waves propagating through the on-board electronic components is especially of concern. A base pressure-time curve derived from a lumped parameter computer code IBHVG2 (Interior Ballistics of High Velocity Gun, version 2) was first used for the study. Because of the difficulty in designing an igniter that can produce hot gases fast enough to evenly permeate charges, transient excitations take place, which result in the base pressure exceeding the chamber pressure while the charge is being ignited and before the projectile moves significantly (*8*). Because IBHVG2 assumes perfect ignition situation, i.e., all charges are ignited at time zero, it lacks the formation of pressure waves and imbalance in the chamber. As a result, the pressure curve from IBHVG2 is monotonically smooth. The pressure wave phenomena can be represented by a pulse in the initial phase, which was investigated after the smooth pressure curve.

In general, high accuracy of base pressure-time prediction has been achieved over the years. Recently, the development of comprehensive multiphase and computational fluid dynamics-based interior ballistics code that can account for primer combustion process has made great strides in interior ballistic (IB) modeling (*9*). It is known that the permeability of the propelling charges and the energy release character of the igniter affect the magnitude and duration of the pressure imbalance early in the ignition phase. The properties of charges and igniters could vary because of manufacturing tolerance, packaging deviation, and changing environmental factors. Consequently, this report adopted 15 Gaussian variables to represent possible variations of base pressures for a selected time period. A considerable number of pressure samples were generated with the Latin Hypercube sampling technique. The sensitivity of the responses of the on-board electronic components to the simulated pressure curves is then studied.

2. Description of EAPS Projectile System

2.1 Geometry of Projectile System

A flare-stabilized sub-projectile test bed is shown in figure 1, which has a length of 275 mm from nose to tail. The diameters of the tail, the body, and the nose are approximately 54 mm, 25.4 mm, and 12 mm, respectively. The sub-projectile body is made of alloy steel and the flare portion of 7075-T651 aluminum alloy. The inside of the steel body is a cavity in the model. Finlets that provide diverting forces are neglected in this study. The coned space in the tail is designed to accommodate a sensor pack where most electronic devices are installed. Figure 2 demonstrates the configuration of the EAPS projectile system. A sabot crown made of nylon is mated to the sub-projectile, which is primarily intended to uphold the in-bore travel position of the sub-projectile. A pusher plate of aluminum wrapped with a nylon obturator is attached to the tail of the projectile, as shown in the figure.

An M1 57-mm gun barrel shown in figure 3 is used to simulate the projectile launch (*10*). We adopted this gun tube for laboratory use by boring (removing) the rifling in the barrel. Consequently, no engraving takes place in the launch, and the spinning of the projectile is therefore ignored. The total length of the gun tube is approximately 2600 mm.

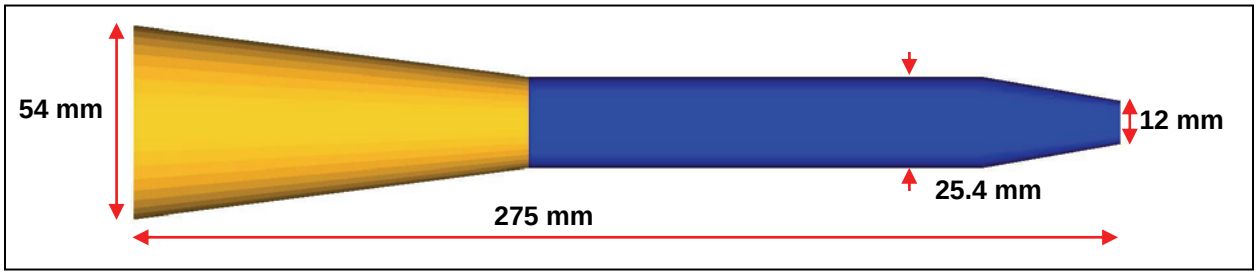

Figure 1. Dimensions of the EAPS sub-projectile.

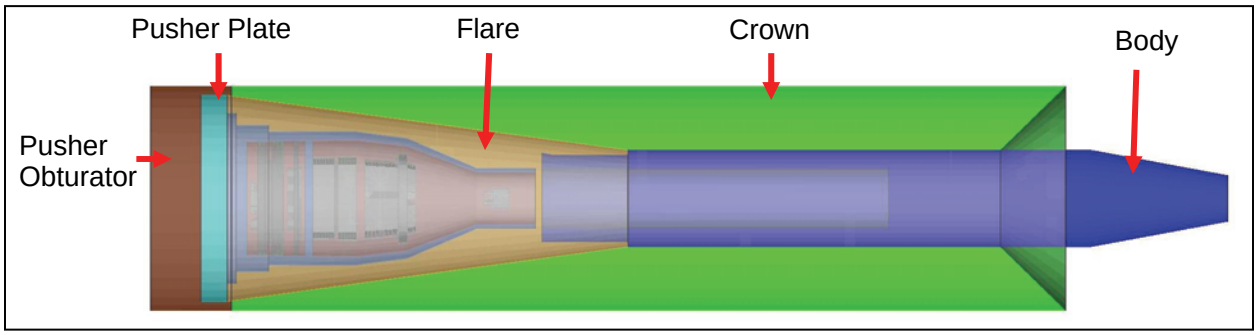

Figure 2. Configuration of the EAPS projectile system.

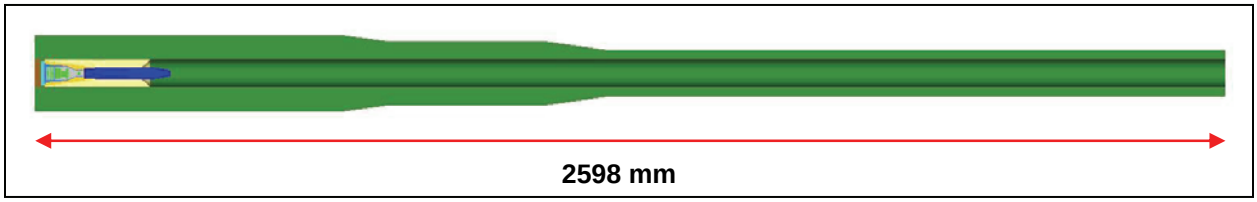

Figure 3. Geometry of the gun barrel.

2.2 Sensor Pack Configuration

An aluminum sensor case shown in figure 4 has a length of 76.2 mm. The container includes two separate parts integrated together. The sensor pack consists of a 2-mm dual row receptacle, an inertial measurement unit (IMU), including an accelerometer and an angular rate sensor, a regulator board assembly, an encoder board assembly, and power supply. All the electronic devices are mounted inside the aluminum container, and the configuration of the sensor pack is shown in figure 5. The remaining space of the container is filled with epoxy potting material. The epoxy encapsulant was used to protect the sensor die against adverse influences from the environment

such as moisture, contaminants, mechanical vibration, and shock. The SolidWorks[1] model of each electronic component is presented in figure 6.

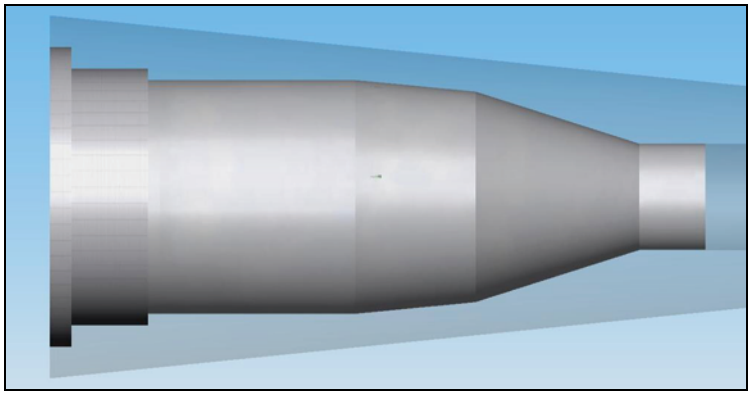

Figure 4. Geometry of sensor pack container.

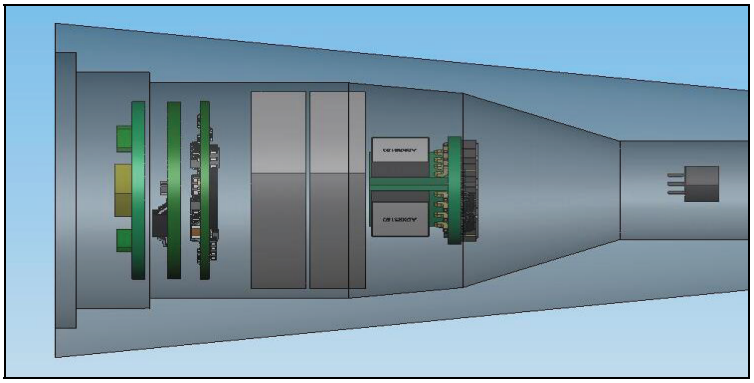

Figure 5. Configuration of sensor pack.

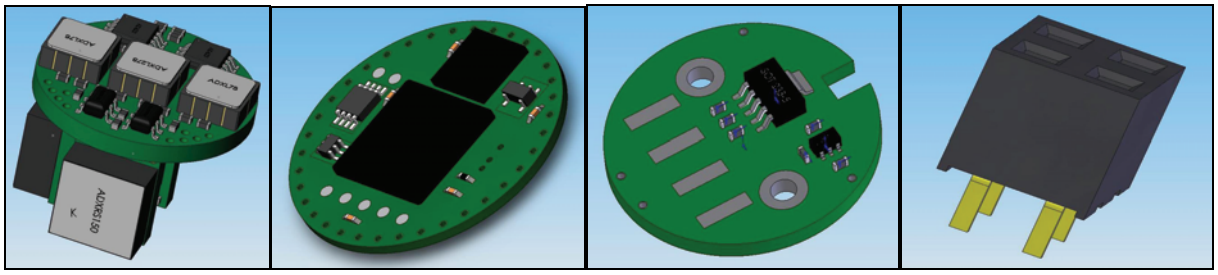

Figure 6. Mounted electronic devices.

2.3 Finite Element Model

Given the geometry of the projectile system, a three-dimensional (3-D) finite element model was created. A cross-sectional view of the projectile model is given in figure 7. The finite element model consists of approximately 220,000 8-node hexahedral solid elements. The detail material

[1]SolidWorks is a trademark of SolidWorks Corporation.

and mechanical properties of the projectile system are provided in table 1. Based on the finite element model, the total mass of the projectile system is approximately 1.26 kg. Because of different attributes, the material and mechanical properties of the composite circuit board assembly are given in table 2, which were extracted from Huang and Newill (*2*). The contact surface was adopted to model the interface between obturator and bore surface. Similarly, the interfaces between the pusher plate and the tail and between the pusher nylon and pusher plate were modeled as surface-to-surface contact. Equivalent nodes were used for the interface between the sabot and the sub-projectile. Tied surface contact was adopted to represent the interfaces between the electronic devices and the potting material. LS-DYNA[2] tool was employed to conduct in-bore dynamic analysis on a Linux Networx Evolocity II cluster at ARL's High Performance Computing Center.

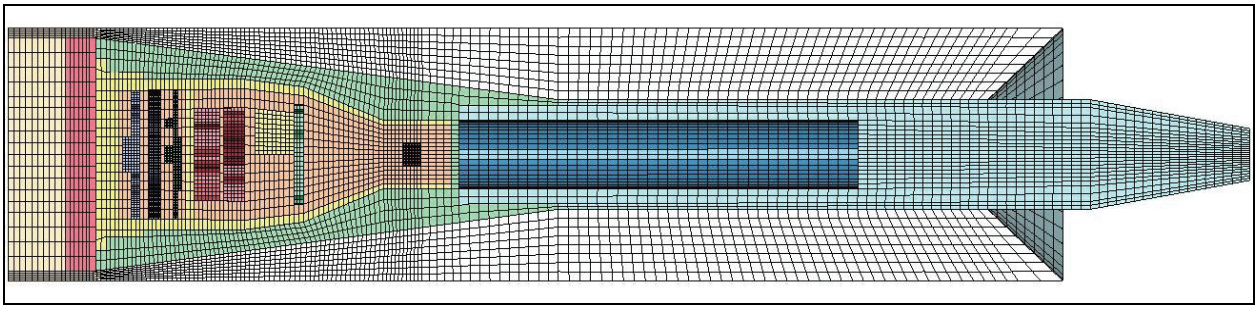

Figure 7. Cross-sectional view of the projectile finite element model.

Table 1. Material and mechanical properties of the projectile components.

Name	**Material**	**Density (kg/m^3)**	**Young's modulus (MPa)**	**Poisson's Ratio**	**Mass (kg)**
Body	Alloy steel	7.45E+03	1.96E+05	0.28	0.484
Flare	Aluminum	2.73E+03	6.90E+04	0.33	0.193
Sensor Pack	Aluminum	2.73E+03	6.90E+04	0.33	6.00E-02
Potting	Epoxy	1.09E+03	2.48E+03	0.35	2.79E-02
Receptacle	Chip	1.16E+03	4.41E+04	0.35	1.62E-04
IMU	Chip	1.16E+03	4.41E+04	0.35	4.06E-03
Battery	-	9.8E+02	6.90E+04	0.3	4.10E-03
Pusher Plate	Aluminum	2.73E+03	6.90E+04	0.33	4.44E-02
Pusher Obturator	Nylon	1.01E+03	3.50E+03	0.4	4.04E-02
Crown (Sabot)	Nylon	1.01E+03	3.50E+03	0.4	0.400

Table 2. Material and mechanical properties of the composite circuit board assembly.

Name	**Material**	**E_L**	**E_T**	υ_{LT}	**G_{LT}**	**Mass**
Regulator board assembly	Composite	2.69E+03	2.15E+03	0.3	9.8E+01	4.37E-03
Encoder board assembly	Composite	2.69E+03	2.15E+03	0.3	9.8E+01	1.26E-03

[2]LS-DYNA is a registered trademark of Livermore Software Technology Corporation.

2.4 Boundary Conditions

Given a 0.9-kg 7-perforation M2 propelling charge, the time history of the chamber and base pressures, which was derived from IBHVG2 interior ballistic code, is given in figure 8. The curves had peak values of 315 MPa and 232 MPa, which took place at 3.2 ms from ignition, for chamber and base pressures, respectively. The base pressure curve was applied to the bottom of the pusher obtuator, and the total excitation duration was 5.15 ms.

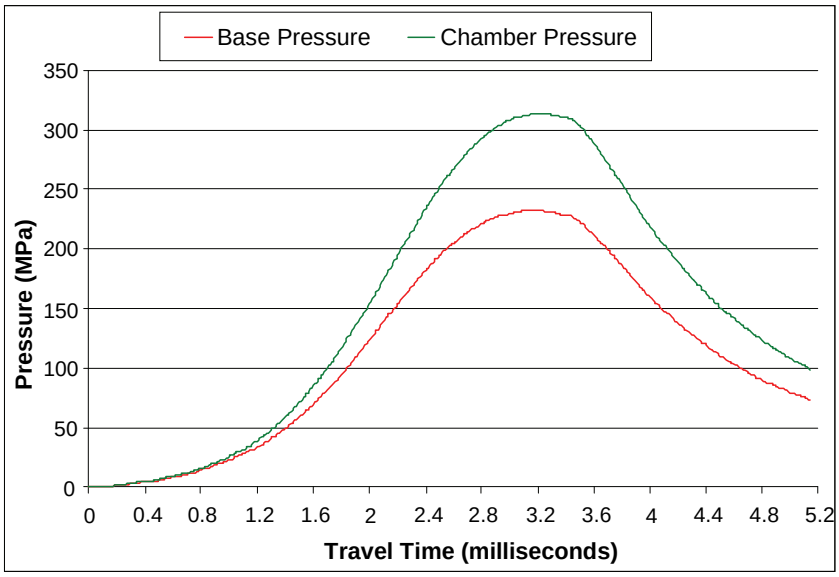

Figure 8. Time history of base and chamber pressures from IBHVG2.

As previously described, the pressure wave phenomenon has been found to be very common for many charges. To simulate the condition, a sinusoidal pulse with a magnitude of 10 MPa for 0.1 ms at the beginning of the ignition phase was used, along with the aforementioned smooth pressure curve. Note that the actual magnitude and duration of the pulse require comprehensive IB modeling. The scale of the pulse being used could be too aggressive. However, the intention was to compare the relative differences in the responses of the on-board electronic devices with and without an initial pulse. On the other hand, a few assumptions would still need to be made in terms of the permeability of the charges and the energy release character of the igniter in IB modeling. Thus, stochastic study was subsequently conducted to account for the uncertainty.

3. Analysis of Overall Projectile System

This section describes in-bore translational and stress responses of the overall projectile system based on the prescribed geometry, material properties, and boundary conditions. The analysis parameters related to the study of pressure waves were outlined. Some unique characteristics of the projectile responses attributable to pressure waves were also illustrated. In addition, undesired

hourglass energy that is generally introduced in explicit solvers because of the use of first order reduced integration elements is discussed. The elements have only one integration point so that they can undergo shear deformation without the introduction of any energy. Most finite element analysis codes that rely on first order reduced integration elements counter this by introducing artificial hourglass energy. In a nutshell, high hourglass energy indicates potential meshing issues that need to be resolved.

3.1 Responses of Projectile System

In-bore travel distance of the projectile versus time is shown in figure 9. It appears that the projectile had no movement until 1.26 ms from detonation, and the total travel distance was 2440 mm. Figure 10 provides the time history of the axial velocity response, which shows a maximum velocity of 1250 m/s at the muzzle. We took the acceleration by averaging the nodal responses in the nose area. A fitting curve given in figure 11 shows a maximum acceleration of approximately 49 kilo-g's (acceleration-to-gravity ratio), which was a desired level for the on-board component survivability assessment.

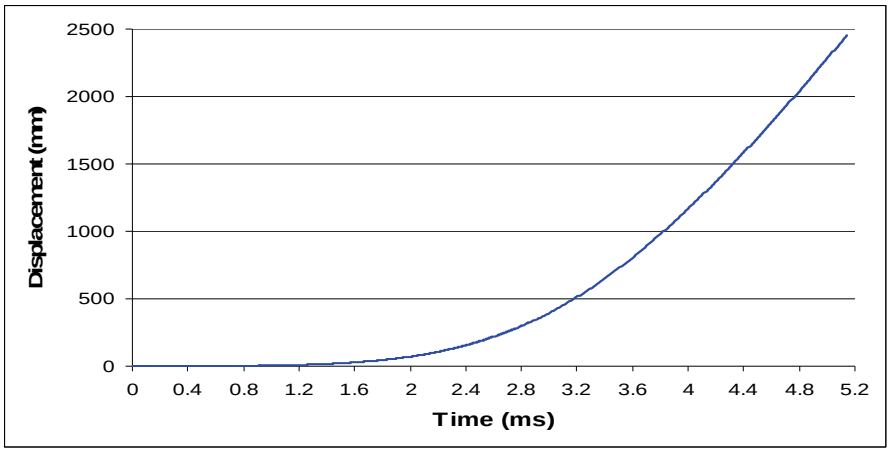

Figure 9. Time history of projectile travel distance.

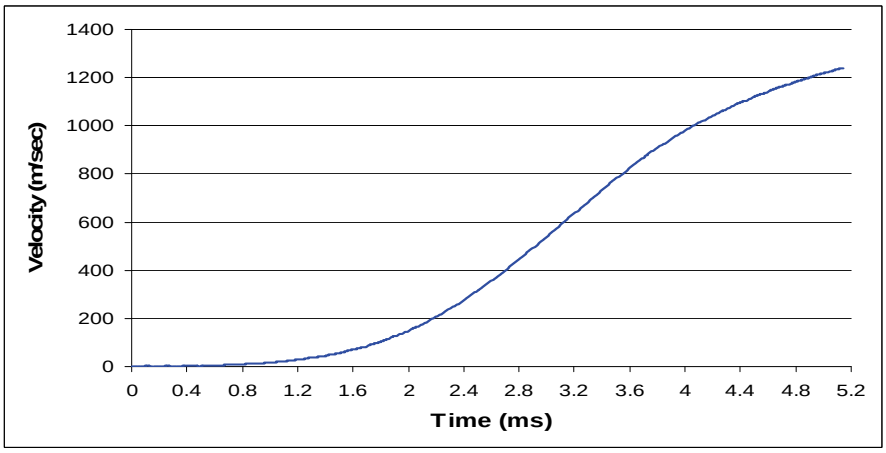

Figure 10. Time history of projectile velocity response.

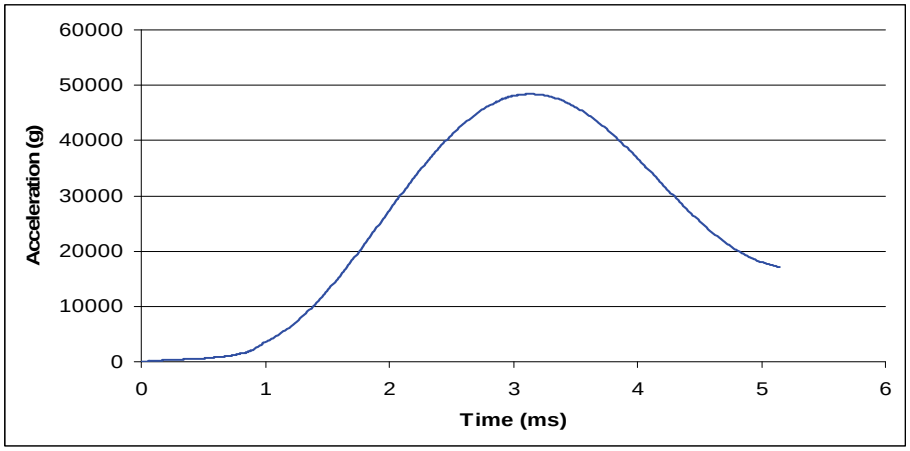

Figure 11. Time history of average acceleration response at projectile nose.

Effective stress responses over the projectile system were first assessed. Figure 12 shows a cross-sectional view of the von Mises stress contours. The highest stress took place at the joint between the body and the flared tail. The stress level of 1118 MPa is acceptable for alloy steel material. Given the overall stress responses, the integrity of the projectile structure should hold. Figure 13 exhibits the plastic strain contours at the pusher obturator. It was found that the nylon obturator experienced large strain of 6% on the joint with the crown. Although no gas leakage is anticipated because of the deformation, possible uneven pressurization may be of concern. The effective stress contours of the sensor pack are given in figure 14. The container for sensor electronics is made of 7075-T651 aluminum, which is subjected to a maximum effective stress of approximately 600 MPa in the corner area as shown. The stress level exceeded the yield strength of the material. The plastic deformation may last only 0.5 millisecond (ms), probably too short to cause a significant damage. However, the location is where the critical IMU device is mounted. Placing additional support around the area inside the structure or increasing the thickness may be suggested to ensure safety.

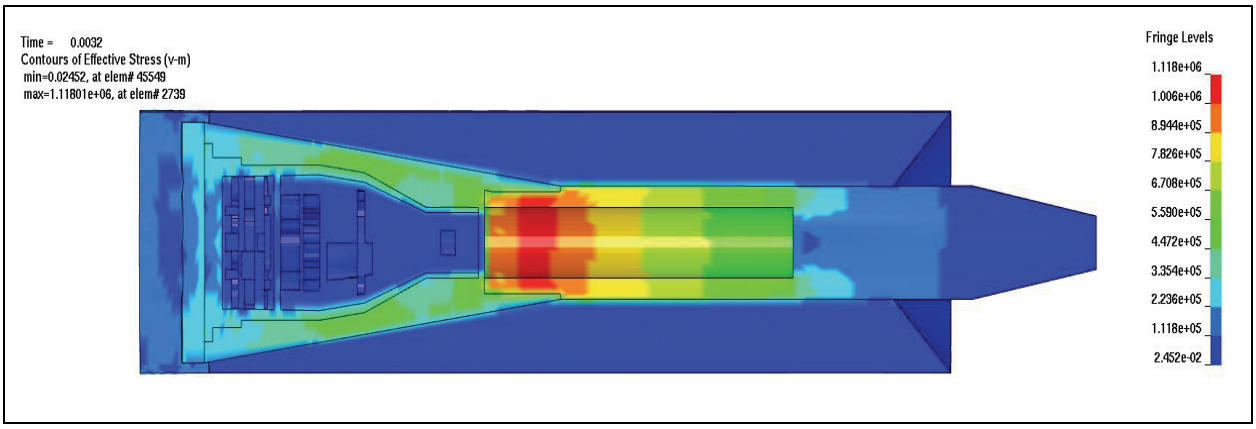

Figure 12. Contours of effective stress responses of the projectile system.

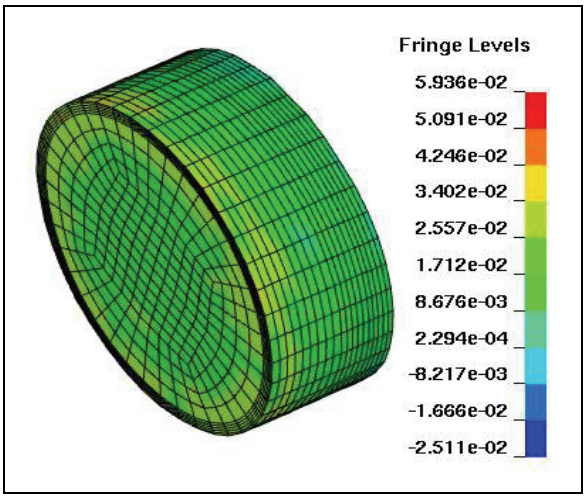

Figure 13. Contours of plastic strain responses of the pusher obturator.

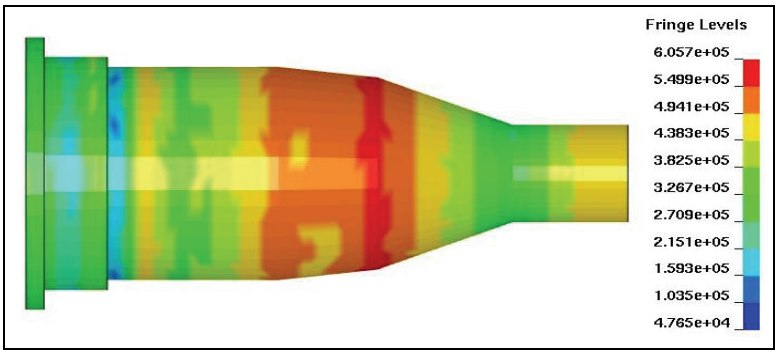

Figure 14. Contours of effective stress responses of the sensor pack.

3.2 Pressure Waves

The speed of a wave traveling through a solid substance could be as high as 5000 m/s. As a result, the time step used to obtain pressure waves must be considerably small. In this study, a time step of 10 μs was adopted for input excitation and output responses. In general, response values will be filtered out if a larger time step is used. Figure 15 demonstrates pressure wave propagation at the tip of the projectile. It appears at a time delay of 0.06 ms, i.e., time required for the wave to travel a distance of approximately 300 mm from the base to the tip. Based on the pressure history, the first few cycles are apparent followed by less predictable oscillations, which could be attributable to reflection, refraction, and interference between different media. In addition, the pressure waves of the projectile body and the battery component were obtained and are shown in figure 16(a) and (b), respectively. The magnitude of the pressure waves at the steel body was found to be approximately 10 MPa—relatively insignificant when compared with the maximum pressure of 350 MPa at the location. Nevertheless, the effect of pressure waves on an on-board component such as the battery is substantially significant. The maximum pressure level has doubled to 600 kPa from 300 kPa when the pressure waves are included. Therefore, caution must be made in the assessment of mounted electronic devices. In practice, a number of packaging technologies for electronic

components applicable to high-g environment have been adopted and summarized by Berman (*11*). In addition, some stress reduction may be accomplished at the chip level for mechanical sensors through the use of special decoupling zones (*12*).

As described, an excitation with an initial pulse along with the base pressure derived from IBHVG2 was also adopted in the analysis. Figure 17(a) and (b) show the pressure responses of the projectile body and the battery component, respectively. A noticeable wave pattern can be seen from the curve of the steel body. As expected, the magnitude of the wave is twice the applied level on the projectile steel body because of the reflection multiplication effect. A peak value of 370 MPa is demonstrated. Unlike projectile body, the impact of the initial pulse on electronic components is less significant. Although pressure waves are apparent and the oscillation is equivalent to the applied excitation frequency in the early phase, the maximum value has no significant increase as opposed to that from prior analysis, which could be because the wave attenuates while propagating through the potting material.

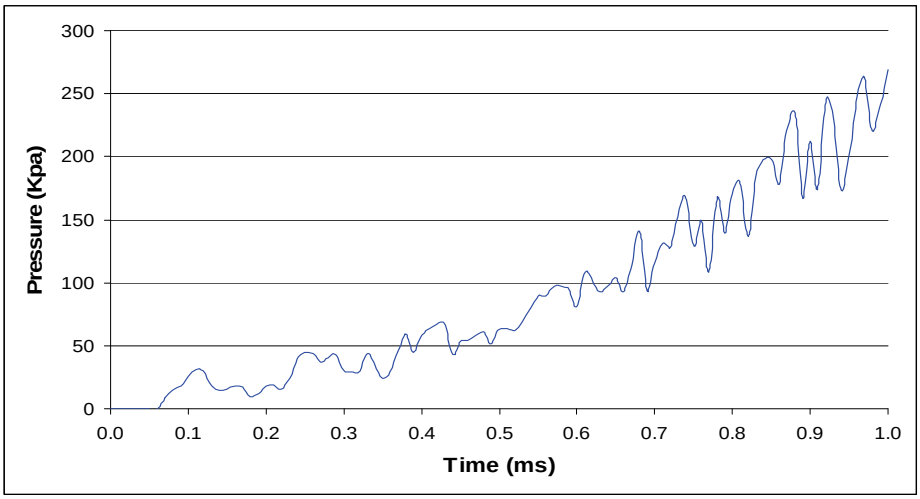

Figure 15. Pressure responses at the center of the projectile nose.

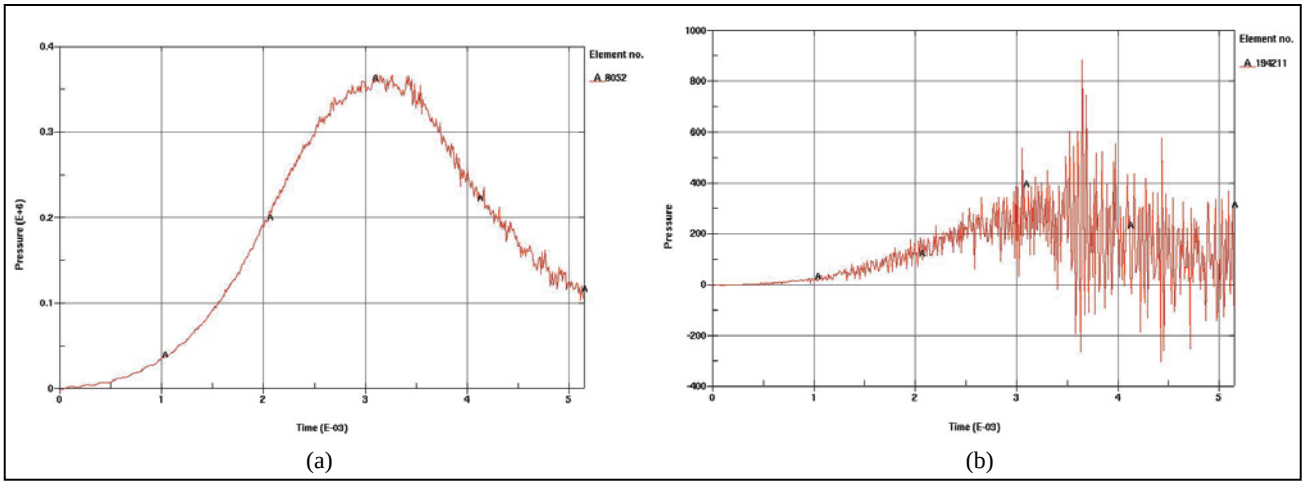

Figure 16. Pressure responses at (a) projectile body and (b) battery.

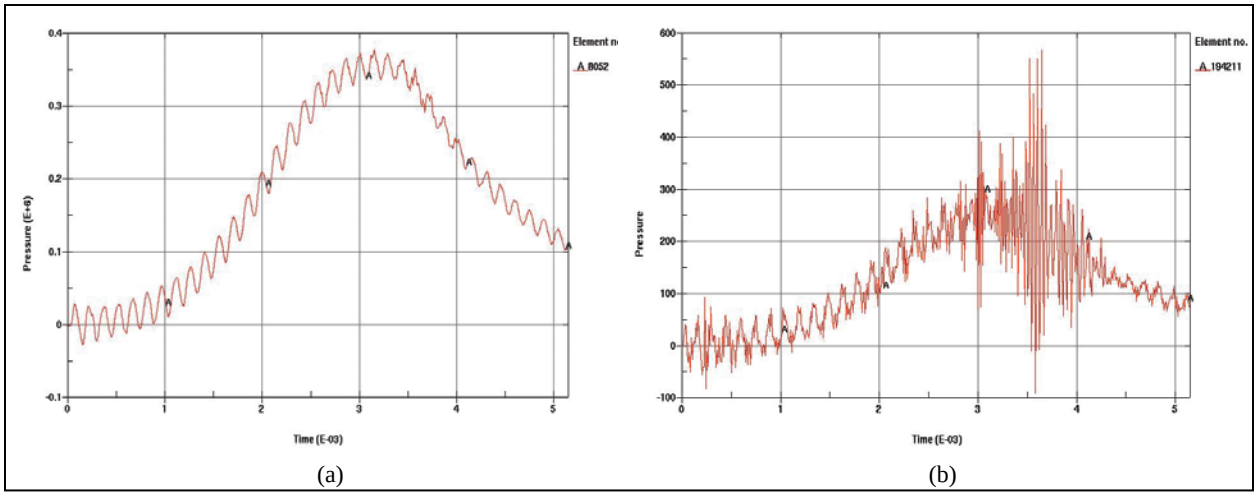

(a) (b)

Figure 17. Pressure responses at (a) projectile body and (b) battery because of an initial pulse.

3.3 Hourglass Energy

In the analysis, significant hourglass modes were found with LS-DYNA default hourglass control. Large shear deformation without the introduction of energy took place, for instance at the pusher obturation as shown in figure 18. The Flanagan-Belytschko stiffness form was subsequently adopted along with various hourglass coefficients ranging from 0.01 to 0.15 (13). The changes of the control have little improvement. The derived hourglass energy was still significant as opposed to the internal energy of the projectile system. Thus, fully integrated solid elements (a more computationally intensive option) were adopted to avoid undesired hourglass energy. The choice of the elements increased the overall stiffness of the model. Nevertheless, the added stiffness increased the maximum von Mises stress response of the projectile system by only 1.9%.

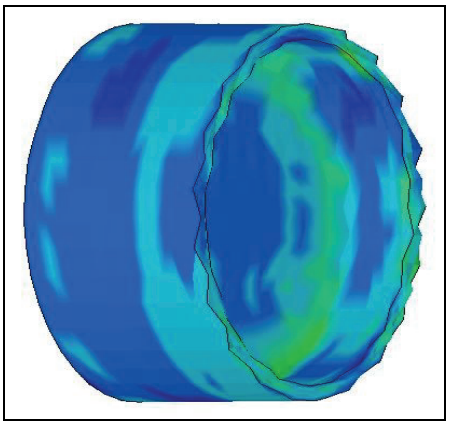

Figure 18. Significant hourglass mode of the pusher obturator.

4. Survivability of On-board Electronic Components

This section focuses on the launch responses of the embedded electronic devices in the projectile system. A variety of failure modes that could occur on electronics is addressed. This section begins with the assessment of yielding failure on the basis of von Mises stress responses. Some electronic components, particularly on the solder joints, encounter a low-cycle fatigue problem because of excess accumulated displacements. Thus, strain responses are also evaluated on the electronic devices. In addition, because of oscillatory forces exerted on the on-board components, potential resonant vibration failure is discussed in this report.

4.1 Stress Responses

The IMU and the 2-mm dual row receptacle units were assessed against von Mises stresses. The stress contours of the IMU are displayed in figure 19(a). The critical stress level appears to be at the ADXRS150 angular rate sensor in which all the required electronics were built on a single chip. Figure 19(b) shows the time history of the von Mises stress response at the device. A maximum value of ~3.0 MPa was derived. Likewise, the stress contours and the stress history are provided in figure 20(a) and (b), respectively, for the receptacle component. A stress level of approximately 3.5 MPa was found. Since most dielectric material has a tensile strength more than 20 MPa, both components were subjected to acceptable stress levels. The epoxy encapsulation may have contributed to the stress mitigation.

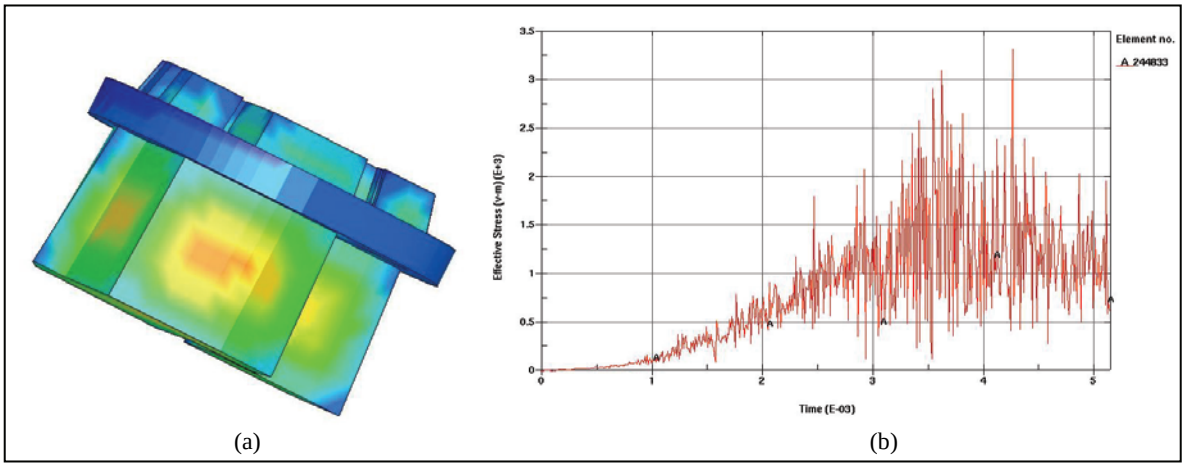

(a) (b)

Figure 19. (a) Effective stress contours of IMU unit; (b) time history of effective stress at an element.

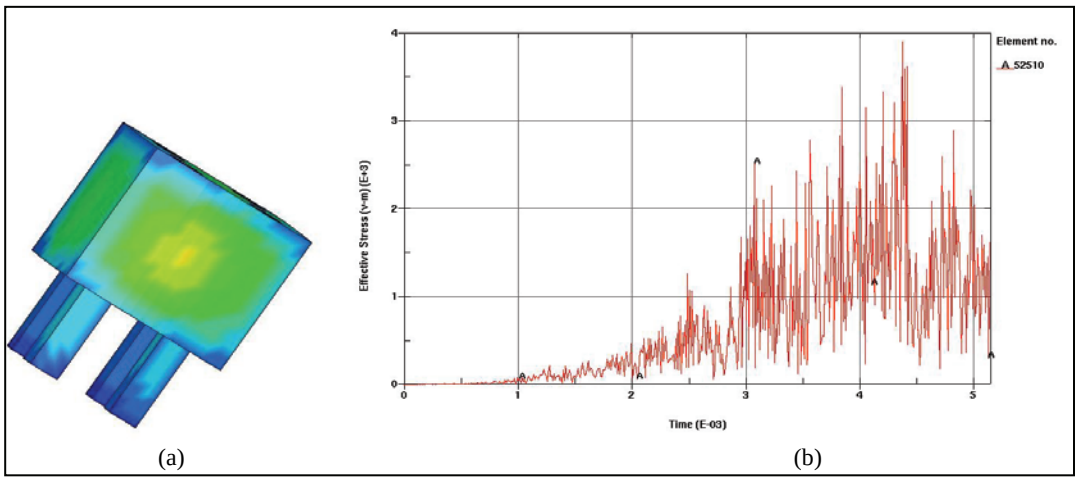

Figure 20. (a) Effective stress contours of receptacle unit; (b) time history of effective stress at an element.

4.2 Strain Responses

Effective plastic strain has been used to evaluate the reliability of electronic components (*14*), particularly in low-cycle fatigue life prediction. Although the details of wiring, resistors, and capacitors were not modeled in the preliminary analysis, the plastic strain responses of the two composite boards at the time when the maximum strain occurred were obtained, which could serve as a baseline for future study at chip level. Figure 21(a) shows the contours of the effective plastic strain response over the encoder board assembly, and figure 21(b) gives the time history of the response at two elements of the component, one at the top surface and the other at the bottom. Because of compression force at the bottom surface and tension at the top, the board was obviously in a bending mode. The maximum strain level was approximately 0.002%, as demonstrated in figure 21(b). Similarly, the response was derived for the regulator board assembly as shown in figure 22(a) and (b). A highest effective plastic strain of 0.004% was obtained on the compression side. The accumulated effective plastic strain could be used for the evaluation of solder joint survivability (*15*).

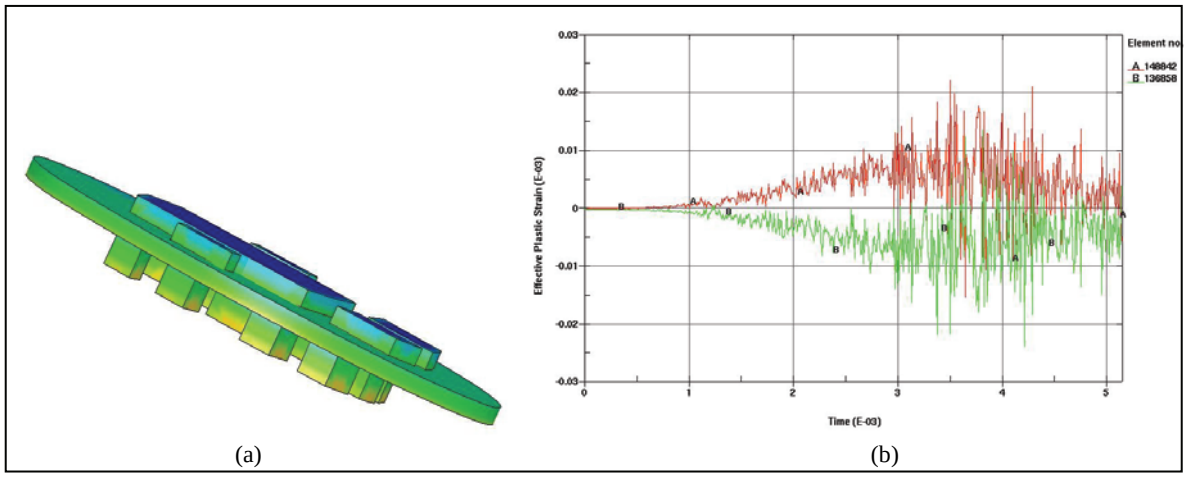

Figure 21. (a) Effective plastic strain contours of an encoder board assembly; (b) time history of effective plastic strain at two elements of the assembly, one at the top and the other at the bottom.

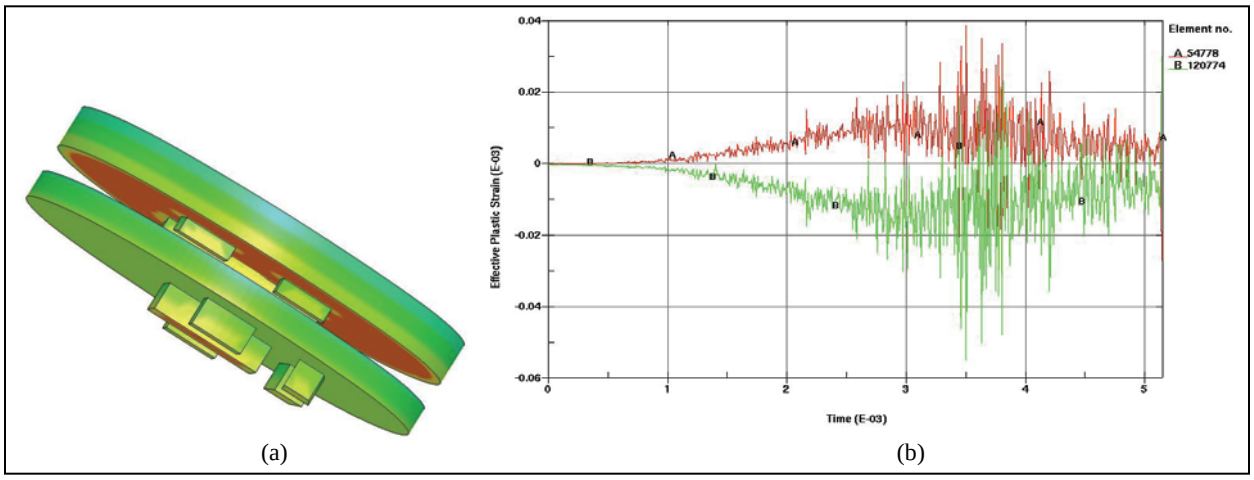

Figure 22. (a) Effective plastic strain contours of a regulator board assembly; (b) time history of effective plastic strain at two elements of the assembly, one at the top and the other at the bottom.

4.3 Resonant Vibration

Because of oscillatory forces, the on-board components need to be verified against resonant vibration. The voltage regulator board was taken as an illustrative example for the analysis. The time history of the pressure applied on the device is given in figure 23(a). The excitation history was converted into frequency domain through fast Fourier transformation, and the result is shown in figure 23(b). Additionally, modal analysis was performed on the regulator board. The first two vibration modes of the regulator board were obtained and are shown in figure 24. The natural frequencies of mode 1 and mode 2 are 20,176 Hz and 20,237 Hz, respectively. From the spectrum, no significant Fourier power was exhibited around the frequency range of 20,000 Hz. The analysis is also extended to the excitation with an initial pulse. Similarly, the pressure responses of the regulator board were derived in both time and frequency domains, and the results are shown in figure 25(a) and (b), respectively. Although the stress responses of the on-board components (attributable to the pressure wave) had little effect, the pattern of the forcing frequency is significantly altered. A dominant frequency of 7,000 Hz was derived as displayed. As a result, large amplitude vibrations attributable to the driving forces are not anticipated. Apparently, the excitation spectrum highly depends on the characteristics of the initial pulse, which warrants more rigorous modeling treatment in interior ballistics.

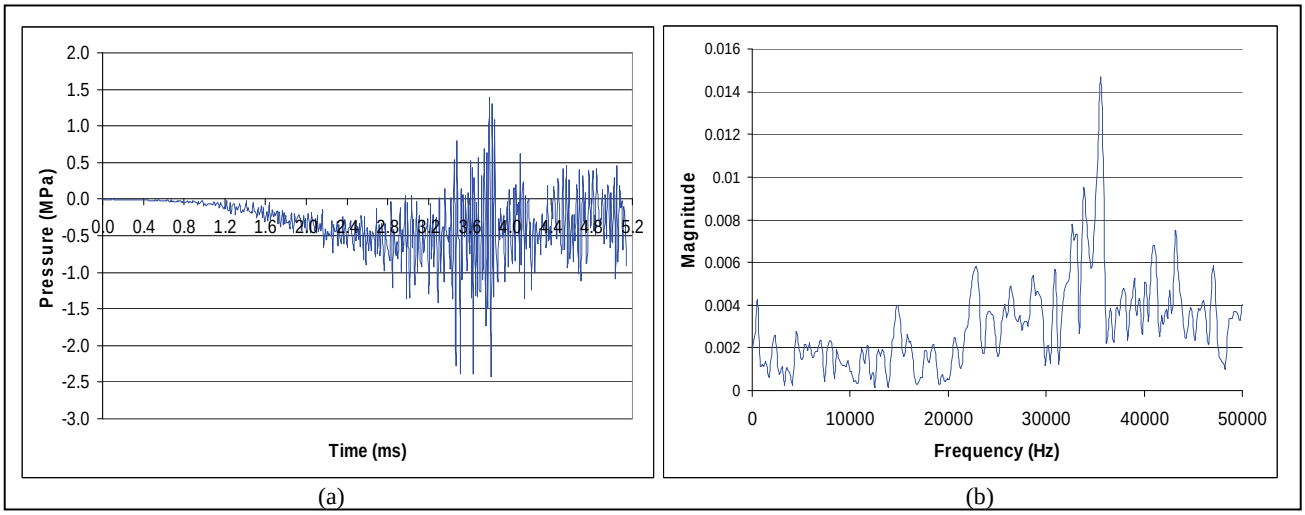

Figure 23. Pressure responses of the regulator board (a) in time domain and (b) in frequency domain.

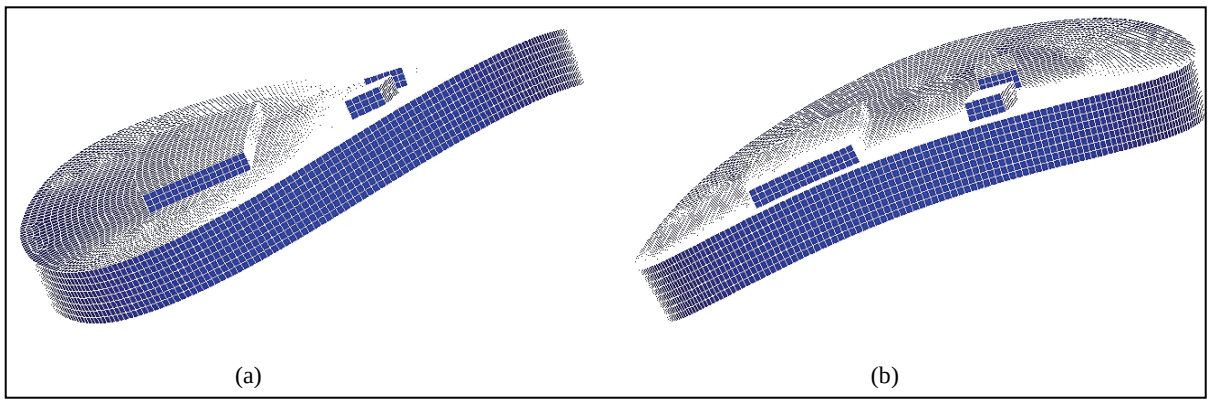

Figure 24. Vibration modes of the regulator board: (a) first mode and (b) second mode.

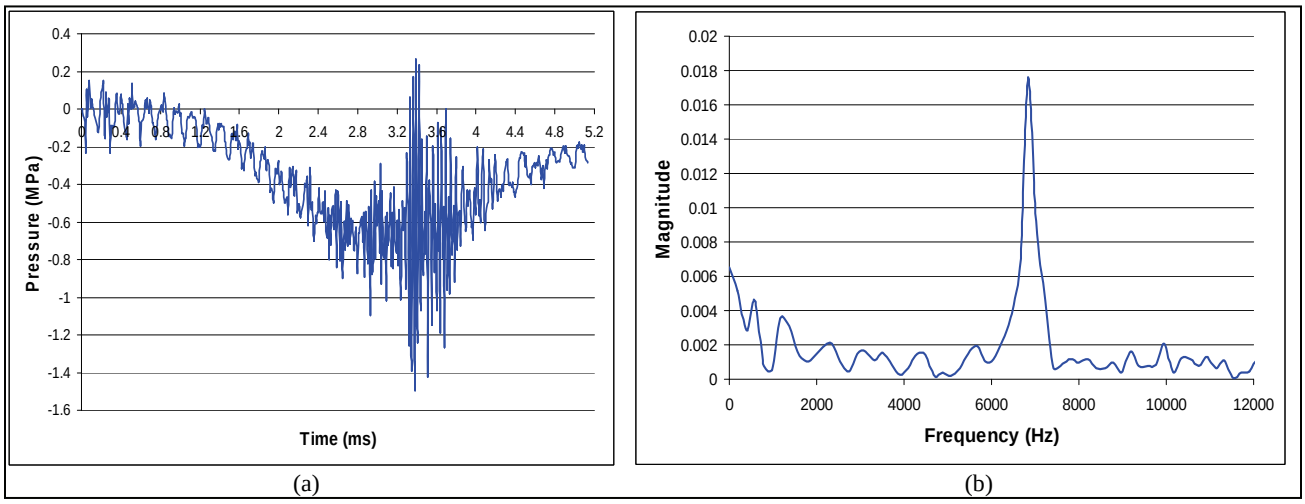

Figure 25. Pressure responses of the regulator board because of an initial pulse (a) in time domain and (b) in frequency domain.

5. Stochastic Modeling of Initial Base Pressure

The aforementioned analysis was based on a deterministic pressure wave model. As previously discussed, the causes of pressure waves potentially involve some uncertain factors that might be better represented by a stochastic model. This section describes the stochastic approach to simulating possible pressure waves that could be triggered during launch. A number of variables representing the pressure level at each time step were chosen for a selected time period. Unlike the direct Monte Carlo simulation method, which may encounter a sample clustering problem, a more effective sampling technique named Latin Hypercube is employed for this study. The detail of the simulation was denoted and the validity of the modeling efforts was discussed. In addition, some issues regarding the base pressure imitation in connection to IB modeling are addressed in this section.

5.1 Latin Hypercube Sampling

Latin hypercube simulation was first proposed in late 1970s (*16*). It is a stratified sampling technique that has been increasingly used over the past decade. It was developed to generate a distribution of plausible collections of parameter values from a multidimensional domain and is often applied in uncertainty analysis. Specifically, when one is sampling a function of N random variables, the range of each variable is divided into M equally probable intervals. The required number of samples is independent of the number of variables, and the sampling scheme is a memory process. Figure 26 illustrates the sampling for two variables. The probability domain of each variable is evenly divided into four intervals, each row/column representing 25% likelihood of occurrence. In general, one must first decide how many sample points to use and must remember for each sample point in which row and column the sample point was taken. This example demonstrates four sample points.

	Variable 2			
Variable 1			X	
	X			
				X
		X		

Figure 26. Illustration of Latin hypercube sampling for two variables.

It was mentioned that pressure imbalance takes place in the chamber while the charge is being ignited and before the projectile moves significantly. The phenomenon is attributed to the non-uniform gas flow among charges, which affects combustion process. A total of 15 Gaussian variables was employed to characterize the pressure noises. Each variable represents the pressure level at one time step (0.01 ms per time step) for the period between 1.16 ms and 1.30 ms from ignition. The base pressure curve in figure 8 serves as a baseline value, and a coefficient of

variation of 5% was adopted for the noise level. A total of 100 Latin hypercube samples was generated for each variable, and the results are provided in appendix A. The histograms of the pressure samples for the time steps 1.16 ms and 1.30 ms (i.e., random variables 1 and 15) are shown in figures 27 and 28, respectively. The pdf and cdf curves on the chart represent probability density and cumulative distribution functions, respectively. The distributions appear to represent the Gaussian population well.

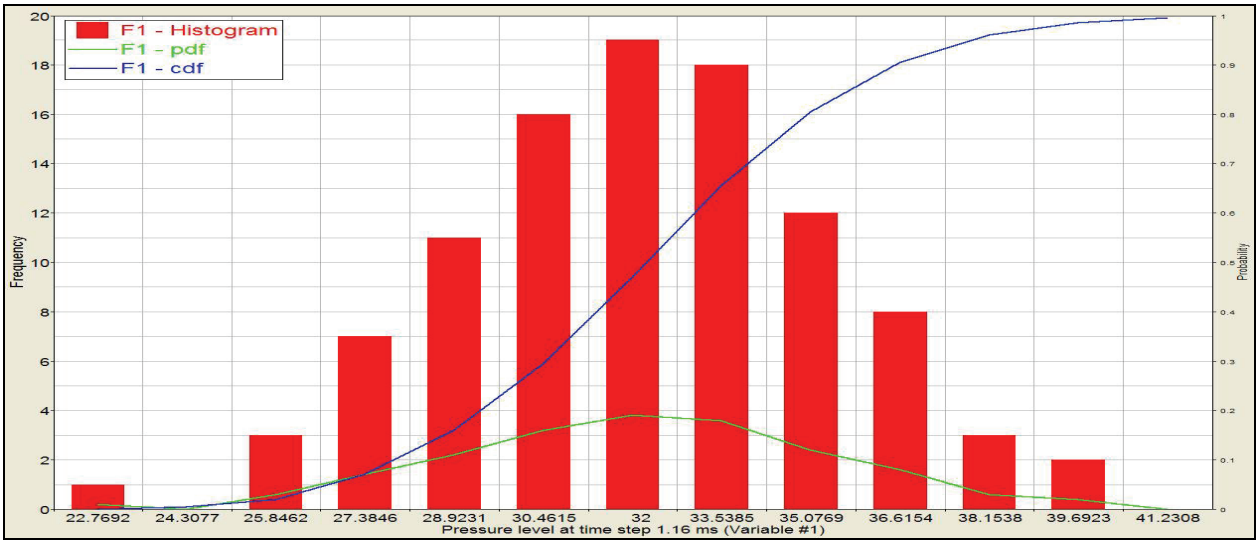

Figure 27. Histogram of pressure level at time step 1.16 ms (random variable 1).

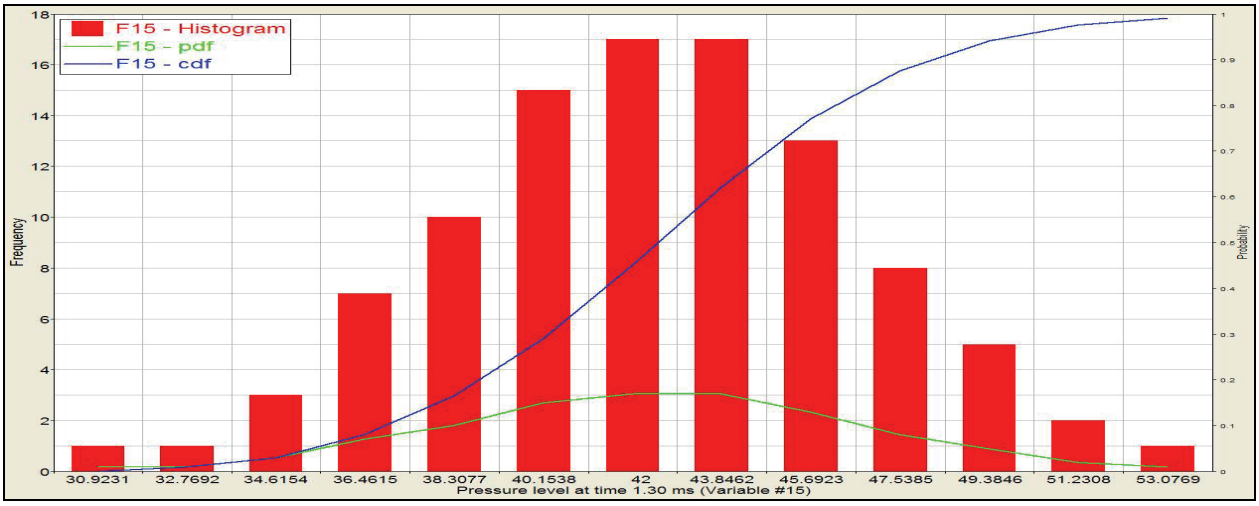

Figure 28. Histogram of pressure level at time step 1.30 ms (random variable 15).

5.2 Simulation of the Base Pressure

Based on the simulated Latin hypercube samples, a total of 100 cases with distinct pressure curves was obtained. For illustration purposes, the pressure history of the first five cases is shown in figure 29. The curve of Case 1, which comes with one major pulse, appears more likely to take

place. In general, high oscillatory pressure distribution is rarely derived from the output of interior ballistic analysis. On one hand, the underlying physical models without the use of sine-wave-like initial and/or boundary conditions are not expected to yield such results. On the other hand, the time interval for observing pressure responses is subjected to the sensitivity of pressure gauges used in laboratory experiments. In other words, it is possible that the current measurement resolution could not unveil this kind of pressure oscillations. Discussion of the detail is beyond the scope of this report.

Regardless of the likelihood of the occurrence of transient excitations, the intention of the study is to gain a better understanding of how sensitive the responses of the EAPS projectile are, especially of the on-board electronic components, to the potential excitation patterns. The sensitivity is evidently critical to the design of the electronic devices. As previously described, the magnitude and duration of the pressure imbalance in the gun chamber at the early combustion phase depend on the permeability of the charges and the energy release character of the igniter. The current application was based on a time period of 0.15 ms, i.e., between 1.16 ms and 1.30 ms from ignition, as shown in figure 29, but the simulation methodology can be extended to the desired duration. The length of the excitation variation does have a significant influence on the true projectile responses. However, the impact on the sensitivity study because of the adjustment of the noise period is expected to be marginal.

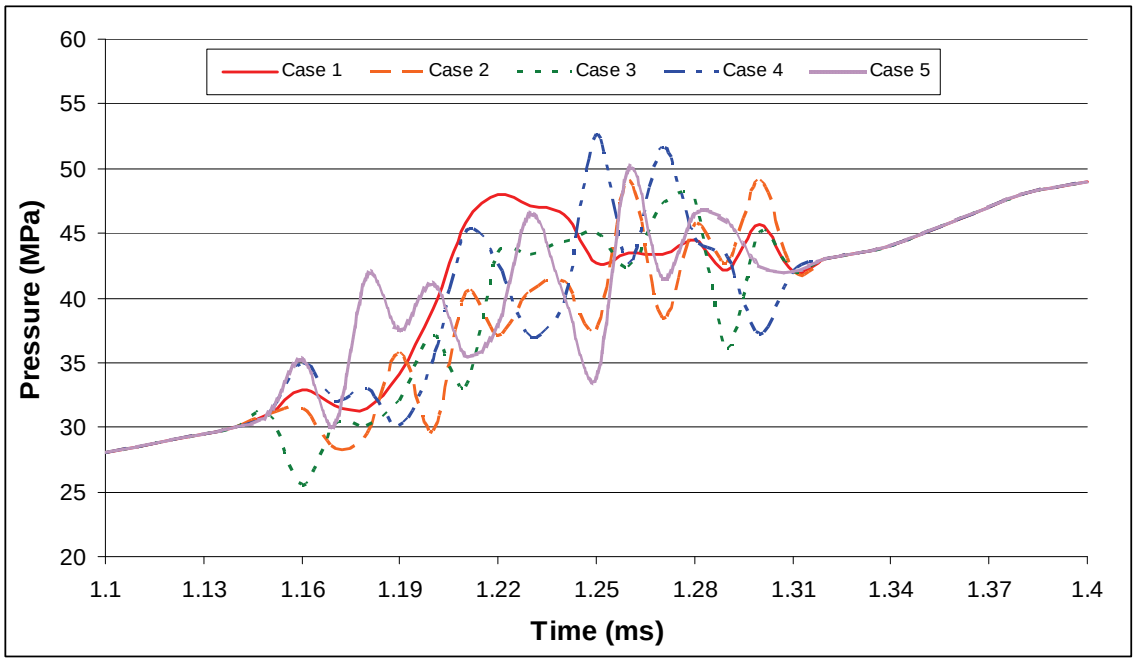

Figure 29. Simulated cases of initial base pressure.

It must be pointed out that the simulation of the initial base pressure does not challenge current IB models. As previously described, the magnitude and duration of the pressure imbalance in the gun chamber at the early combustion phase depend on the permeability of the charges and the

energy release character of the igniter. The proposed perturbation merely represents possible variations in the properties of the charges and the igniter because of changing factors such as temperature, humidity, granular shape variations of propelling charges, packaging deviations of each propellant load, etc. Furthermore, the validity of the sensitivity study must rely on the accuracy of the pressure curve derived from existing IB models such as IBHVG2 or NGEN (next generation multidimensional IB codes). A simple mathematical expression may explain the dependency. Given that

$$\sigma = f(p(x,t))$$

where σ stands for component stresses and p stands for a pressure function, the sensitivity of the stress function to the pressure can then be expressed as

$$\frac{\partial f}{\partial p} = \left(\frac{\partial \sigma}{\partial t}\right) / \left(\frac{\partial p}{\partial t}\right)$$

that is, the rate of change of stress divided by the rate of change of pressure. Since function f is difficult to derive explicitly, the sensitivity is therefore studied computationally. As a result, rigorous modeling to simulate closer-to-reality ignition situation, which is being pursued as part of the development of NGEN code, should be warranted to ensure a better prediction on the pressure change rate for this study.

6. Stochastic Analysis of Projectile System

6.1 Stochastic Results

The 100 base pressure samples derived from the Latin hypercube simulation were applied to the projectile system. Each sample required an individual finite element analysis. For illustration purposes, the time history of the von Mises stress responses at the steel body for the first five cases is given in figure 30. It can be seen that the transient excitation that occurred in the early phase of ignition had little influence in the vibrating frequency of the stress waves at this location. In addition, the magnitude of the maximum stress response had only a slight difference from one case to another throughout the overall travel period.

Furthermore, the stress responses were assessed at on-board electronic devices. Figures 31, 32, and 33 demonstrate the time history of the von Mises stress at the IMU (element #244826), encoder board (element #136033), and regulator board (element #54784), respectively. It is shown that the effective stresses of the electronics are highly sensitive to the initial excitation patterns because of the considerable discrepancy in the response curves. The maximum effective stresses of the IMU unit closely agree among the cases, but the occurrence time deviates. For the responses of the encoder and regulator boards, the maximum stress values differ significantly. For instance, figure 33

depicts a highest stress of 4 MPa for cases 1 and 2 and only 2.7 MPa for the other three cases at the regulator board. The critical response time at on-board components appears to be independent of the time when the maximum base pressure took place, i.e., 3.2 ms from ignition.

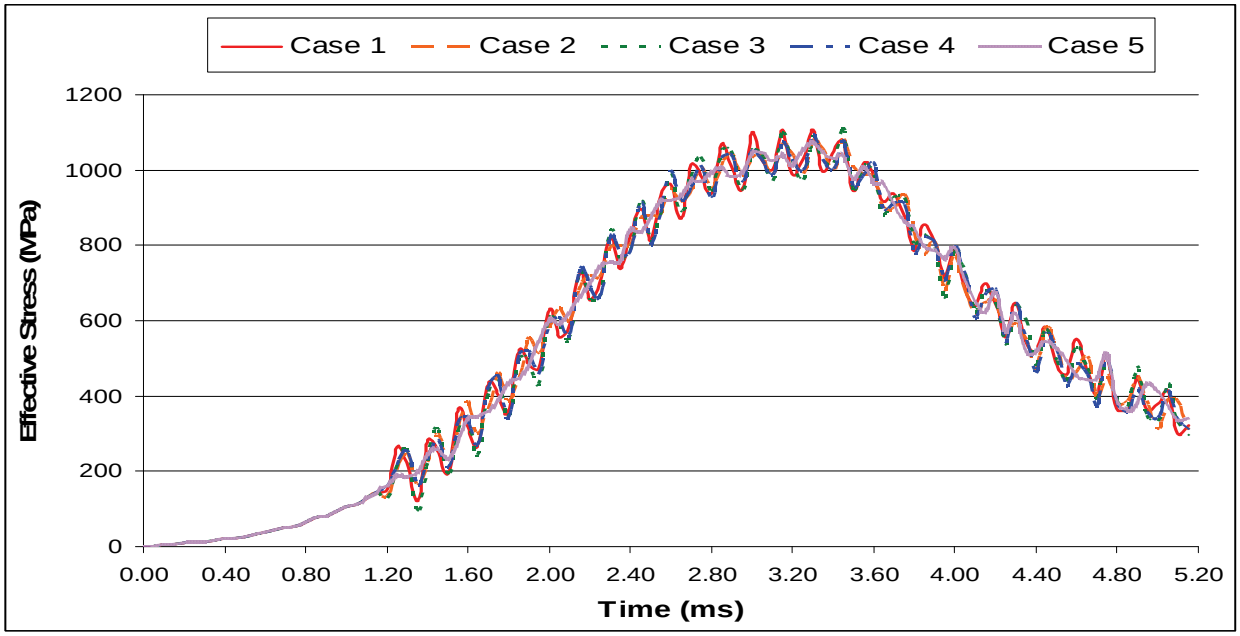

Figure 30. Time history of effective stress at projectile body for the first five cases.

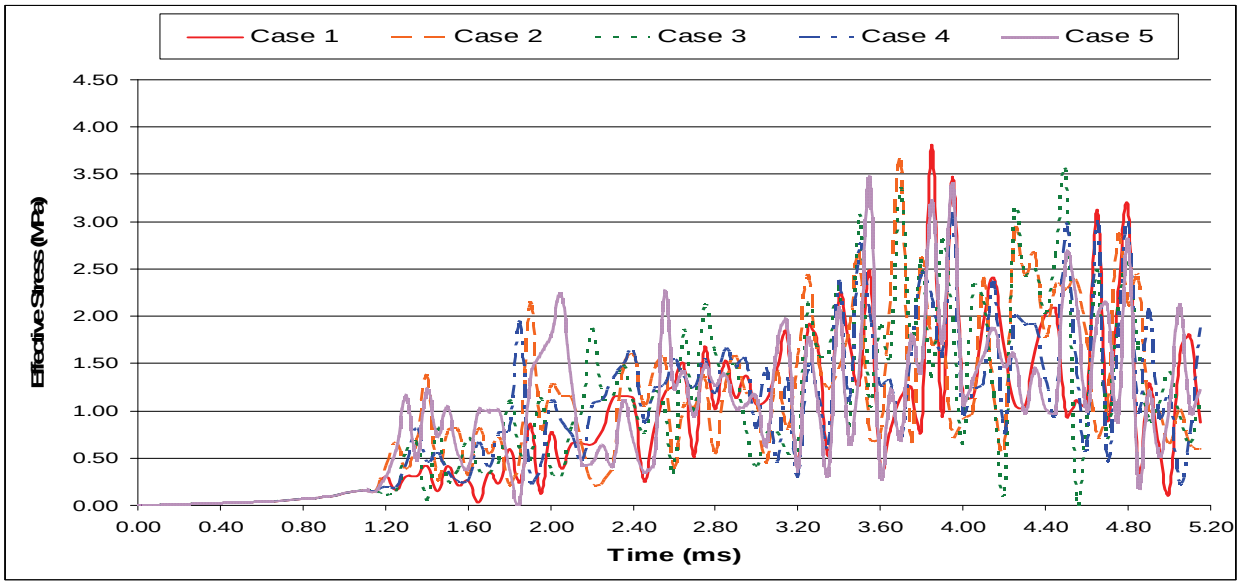

Figure 31. Time history of effective stress at IMU for the first five cases.

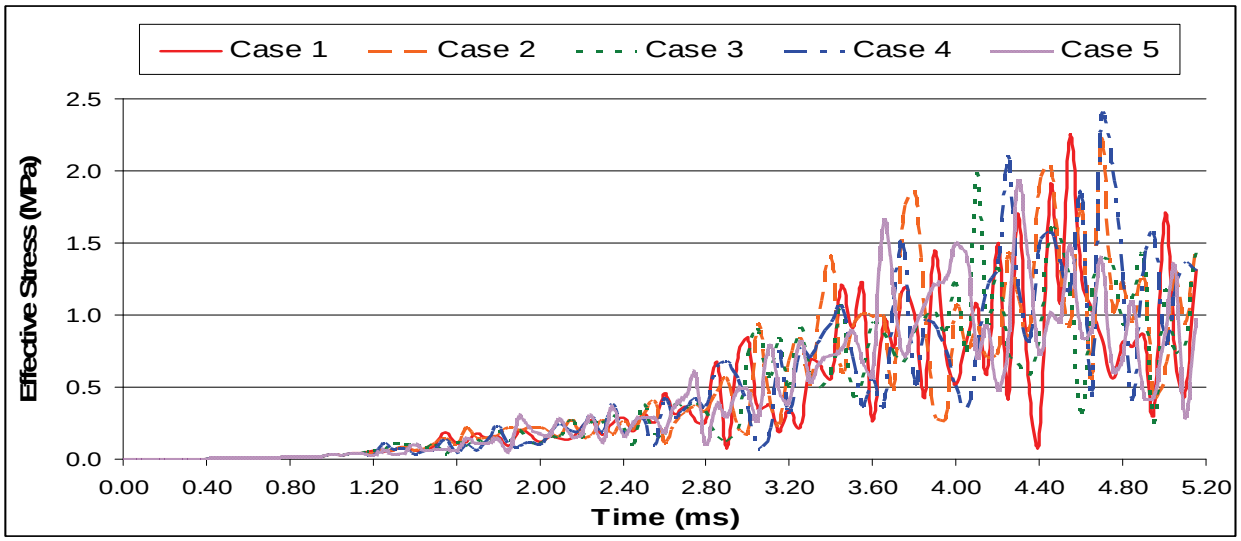

Figure 32. Time history of effective stress at encoder board for the first five cases.

The study of the effective stress response is extended to space domain. The response contours of the regulator board at the time of 3.2 ms from ignition for the cases 1 and 2 are given in figure 34(a) and (b) respectively. The boards yielded maximum stresses of 2.74 MPa and 3.53 MPa correspondingly. Unlike the projectile steel body, the locations where the maximum stress occurred vary, and the response patterns appear to be diverse at the time instant. As described, the highest in-bore stress level of the component could happen at other time steps during travel.

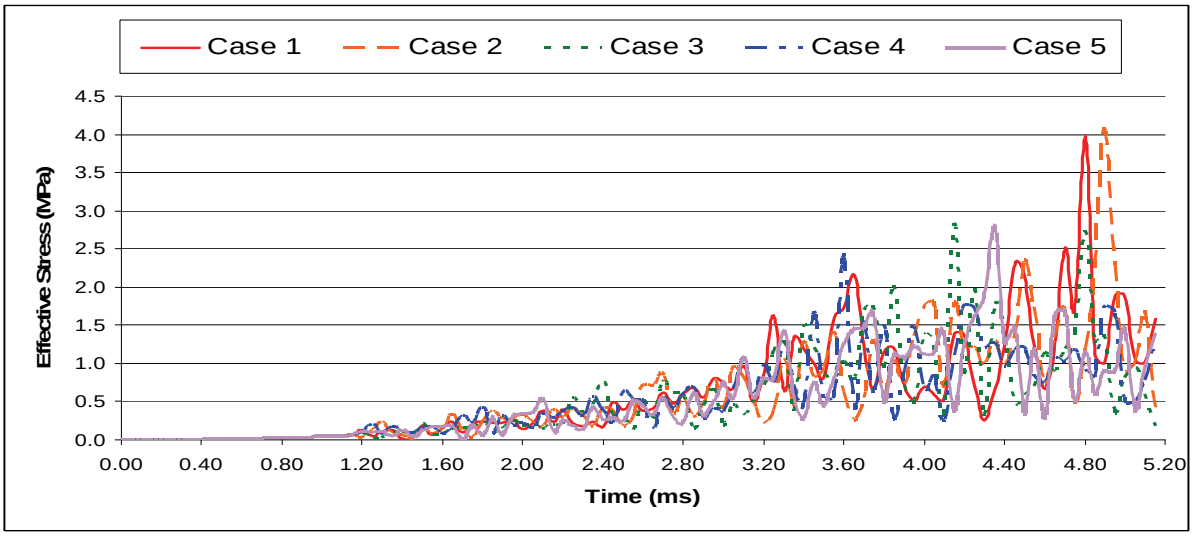

Figure 33. Time history of effective stress at regulator board for the first five cases.

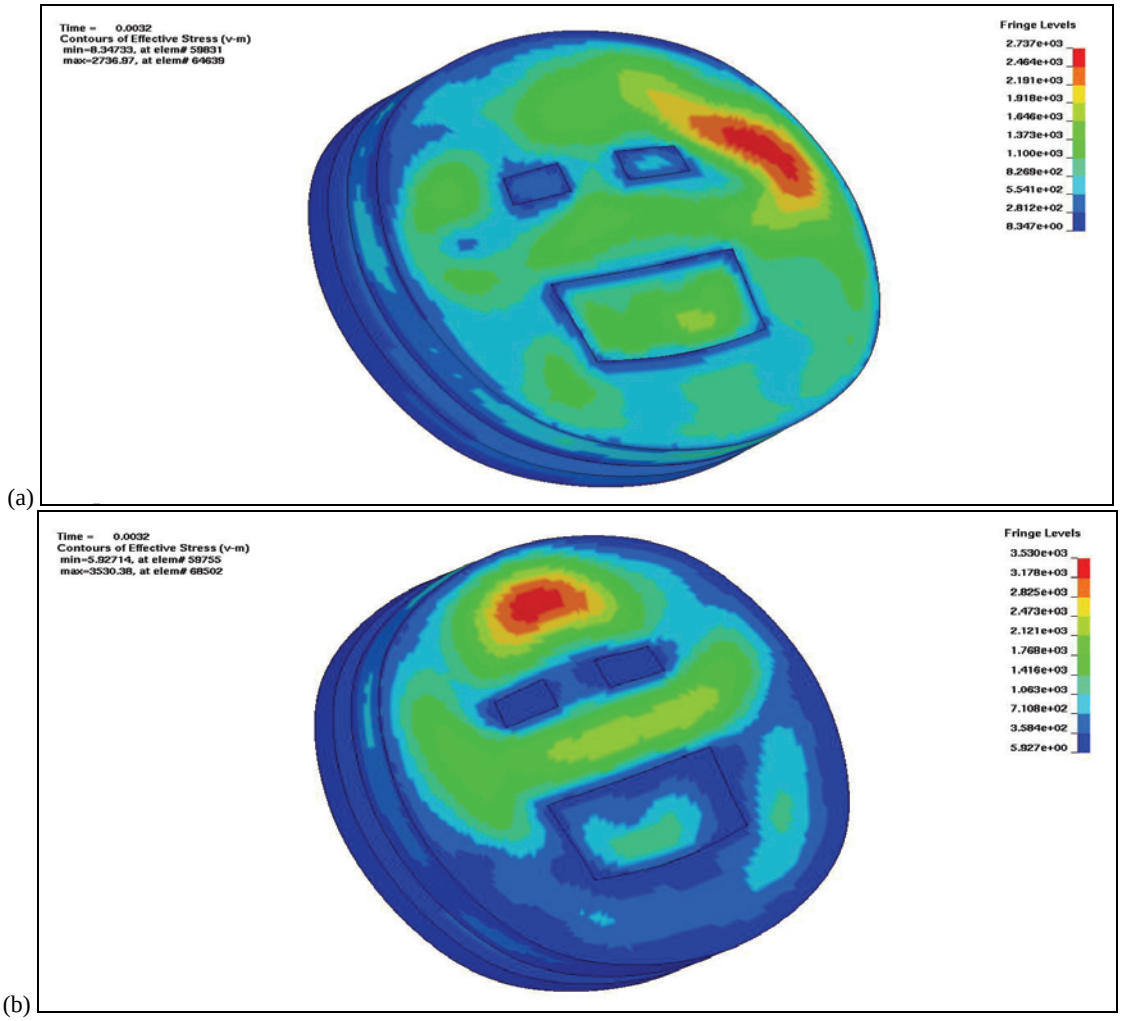

Figure 34. Effective stress response contours of regulator board at 3.2 ms for (a) Case 1 and (b) Case 2.

6.2 Statistical Summary

Stochastic results of the first five cases were demonstrated in the previous section. The overall response statistics of the projectile system subject to the 100 distinct excitations are summarized in table 3. An element was chosen for each of the pusher plate, steel body, IMU, encoder board, regulator board, and receptacle components. The mean, standard deviation, coefficient of variation, minimum, and maximum of the von Mises stresses of the selected elements were derived. The mean stress of the aluminum plate is equivalent to the applied base pressure level. The stress range of the projectile body is insignificant compared with the average value. All the stresses of the on-board electronic devices exhibit a high coefficient of variations (more than 10%), which indicates that the responses are fairly sensitive to the simulated base excitations. Nevertheless, the IMU unit that is to withstand a highest maximum stress of 5.1 MPa should survive. Effective plastic strains, which could be used to predict low-cycle fatigue life, were also obtained on the circuit board surfaces. Expectedly, the strain responses disperse as much as the stresses. An average of the axial velocity of 1243 m/sec was computed at the projectile nose. Because of the

substantially low coefficient of variation, the effect of the transient excitations on the velocity response appears to be marginal.

Table 3. Statistical summary of projectile responses to stochastic excitations.

Response	Location	Mean	Std. Dev.	Coef. of Var. (%)	Min.	Max.
von Mises Stress (Mpa)	Aluminum pusher	270	21.7	8.1	230.0	333.1
	Steel body	1092	18.8	1.7	1041	1136
	IMU	3.82	0.47	12	2.99	5.10
	Encoder board	2.30	0.39	17	1.67	3.63
	Regulator board	2.96	0.65	22	1.78	4.83
	Receptacle	3.57	0.36	10	2.85	4.49
Effective plastic strain (%)	Regulator board	1.31E-03	2.38E-04	18	8.1E-04	1.94E-03
	Encoder board	1.20E-03	2.92E-04	24	6.63E-04	2.08E-03
Axial velocity (m/sec)	Projectile nose	1242.9	0.72	5.76E-02	1240.5	1244.4

The distribution of the von Mises stress response is further studied at component level. Histograms of the effective stresses of the IMU and the receptacle units are given in figures 35 and 36, respectively. Both distributions are close to Gaussian but are slightly right skewed. The means of the response are 3820 KPa and 3570 KPa for the IMU and the receptacle, respectively. Note that the overall energy of each case yielded from simulation of transient excitations is equivalent to the baseline pressure curve since a Gaussian process is adopted. The scatter of the stress response is attributed to the variations of the magnitude and duration of momentary agitation. The high sensitivity that is critical to survivability study should warrant rigorous modeling in the determination of pressure waves in the early launch phase.

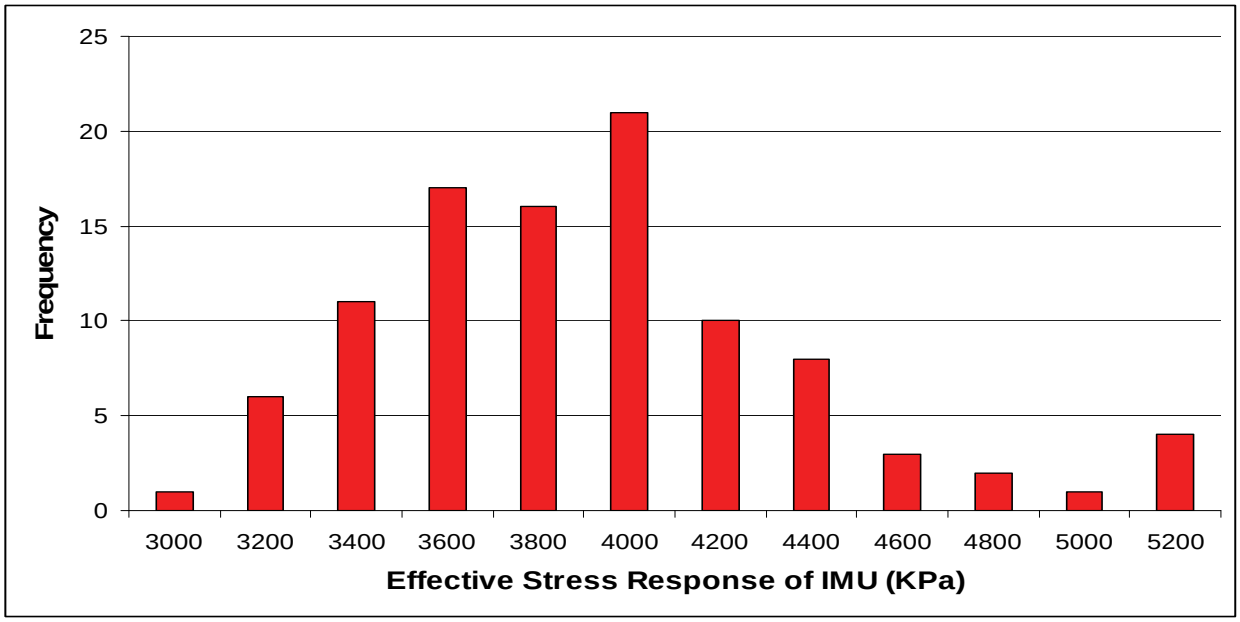

Figure 35. Histogram of stochastic effective stress responses of IMU device .

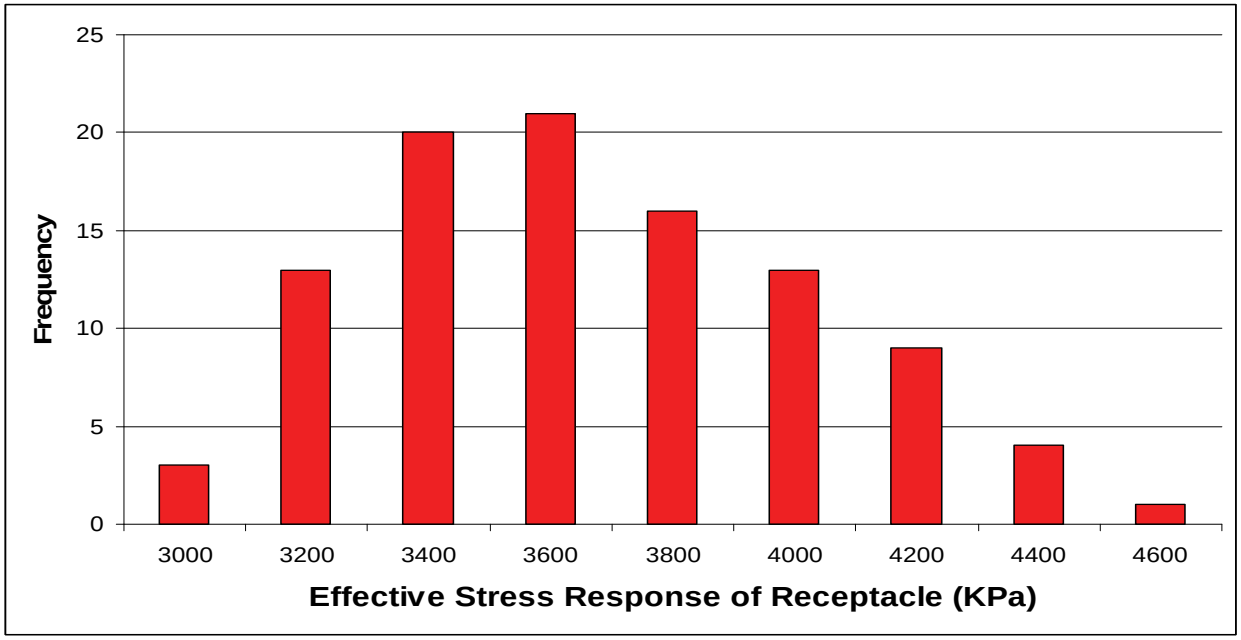

Figure 36. Histogram of stochastic effective stress responses of receptacle unit.

7. Summary and Conclusions

A preliminary survivability study for a test-bed projectile that was designed to accommodate required guidance, navigation, and control devices was conducted. A 3-D finite element model that included some of the major electronic components, such as an accelerometer, an angular rate sensor, a regulator board assembly, an encoder board assembly, a receptacle and batteries, was generated. The on-board components that are expected to function after they exit a gun barrel must be ensured to withstand a high-g hardened environment. The 57-mm precision-guided projectile system was subjected to a pressure load as high as 232 MPa for a short period of time at launch. A pressure curve derived from IBHVG2 was first used for the launch simulation. Because pressure waves have been found to be a very common effect for many propellant charges, the study was then extended to the boundary condition that has an initial sinusoidal excitation in conjunction with the original pressure curve.

Overall stress responses of the projectile system were assessed against structure integrity. The computed effective stresses suggest that no catastrophic failure should take place. Some plastic defor-mation was found to occur at the corner of the container for sensor devices. This location in which the IMU unit was mounted is critical, and therefore, some strength reinforcement is recommended. Stress waves that propagate through the projectile system during launch were identified. Because of the wave reflection multiplication effect, the augmentation of stress response could be signifi-cant to the overall projectile survivability. At the component level, the

effect of pressure waves was proved to be noteworthy to the mounted electronics. The device of the ADXRS150 angular rate sensor, which is subjected to the maximum stress level, was found to be the critical area of the IMU component. However, as far as yield failure is concerned, the device should survive on the basis of the tensile strength of most dielectric material. The effective plastic strains on the surfaces of the two composite circuit boards, i.e., the encoder board and the regulator board, were obtained. The responses could be used to predict low-cycle fatigue failure of solder joints. Furthermore, resonant vibration attributable to oscillatory pressure excitation was evaluated. The structure-excitation interaction was solved in frequency domain. An illustrative example of the voltage regulator board demonstrated no resonance concern.

Finally, because of the difficulty of designing an igniter that can produce hot gases fast enough to uniformly permeate propelling charges, transient excitations take place while the charge is being ignited and before the projectile moves substantially. The permeability of the charges and the energy release character of the igniter, which determine the magnitude and duration of transient excitations, generally involve some unpredictable nature. A total of 15 Gaussian variables and the Latin hypercube sampling technique were adopted to model the variations of the momentary agitation on the projectile system in the early launch phase. Through rigorous simulations, i.e., 100 cases, the sensitivity of the responses of the on-board components to the initial pressure waves was investigated. It was found that the responses of the electronics are highly susceptible to the applied excitation patterns. The time history of the effective stresses of some on-board units was discussed for the first five representative cases. The scatter distributions of the stress responses were also outlined. In addition, some statistical quantities that further demonstrate high responsiveness to the stochastic excitations are summarized. Although the detail of wiring, resistors, capacitors, solder joints, etc., was not modeled in this preliminary analysis, the responses on the electronic devices may serve as a baseline for future study, which is quite important since micro-electromechanical systems have been increasingly adopted for military applications.

8. References

1. Brown, G.; Davis, B.; Hepner, D.; Faust, J.; et al. Strap-Down Microelectromechanical (MEMS) Sensor for High-G Munition Applications. *IEEE Transactions on Magnetics* **2001**, *37* (1), 336–342.

2. Huang, X.; Newill, J. *In-Bore Dynamic Analysis of the SCORPION Projectile*; ARL-TR-3048; U.S. Army Research Laboratory: Aberdeen Proving Ground, MD, September 2003.

3. Soencksen, K. Aerodynamic Characteristics of a 120-mm M865 Projectile Containing on-Board Sensor System. *Proceedings of AIAA Applied Aerodynamics Conference*, Anaheim, CA, June 2001.

4. Wilson, M. *ONBORD (On-board Navigation of Ballistic Ordnance): Gun-Launched Munitions Flight Controller*; ARL-TR-3210; U.S. Army Research Laboratory: Aberdeen Proving Ground, MD, August 2004.

5. Peregino, P.; Bukowski, E. *Development and Evaluation of a Surface-Mount, High-G Accelerometer*; ARL-TR-3331; U.S. Army Research Laboratory: Aberdeen Proving Ground, MD, September 2004.

6. Powers, B.; Hopkins, D. *Evaluation of the Submodeling Technique for Analyzing Electronic Components*; ARL-TR-3627; U.S. Army Research Laboratory: Aberdeen Proving Ground, MD, October 2005.

7. Chew, H. B.; Guo, T. F.; Cheng, L. Modeling Adhesive Failure in Electronic Packages. *IEEE Electronics Packaging Technology Conference* **2006**, 787–792.

8. Nusca, M. Personal Communications, Army Research Laboratory, Aberdeen Proving Ground, MD, April 2008.

9. Nusca, M. *High-Performance Computing and Simulation for Advanced Armament Propulsion*; ARL-TR-3215; U.S. Army Research Laboratory: Aberdeen Proving Ground, MD, June 2004.

10. Silsby, G. *Safety Assessment – 57 mm Smooth Gun*; In-house Memorandum Report, Unpublished; U.S. Army Research Laboratory: Aberdeen Proving Ground, MD, August 1995.

11. Berman, M. *Electronic Components for High-g hardened Packaging*; ARL-TR-3705; U.S. Army Research Laboratory: Aberdeen Proving Ground, MD, January 2006.

12. Elwenspoek, M.; Wiegerink, R. *Mechanical Microsensors*; Springer-Verlag Berlin Heidelberg, 2001.

13. LS-DYNA Keyword User's manual, version 970, Livermore Software Technology Corporation, April 2003.

14. Ramakrishna, G.; Pucha, R.; Sitaraman, S., "Micro-scale Plasticity Effects in Microvia Reliability Analysis", IEEE, Electronic Components and Technology Conference, 2002.

15. Lin, Y. C.; Chen, X.; Liu, X.; Lu, G-Q. Effect of Substrate Flexibility on Solder Joint Reliability. *Journal of Microelectronics Reliability* **2005**, *45* (1), 143–154.

16. McKay, M. D.; Conover, W. J.; Beckman, R. J. A Comparison of Three Methods for Selecting Values of Input Variables in the Analysis of Output from a Computer Code. *Technometrics* **1979**, *21*, 239–245.

INTENTIONALLY LEFT BLANK

Appendix A. Latin Hypercube Simulation of Initial Base Pressure (MPa)

Run	Variable 1	Variable 2	Variable 3	Variable 4	Variable 5	Variable 6	Variable 7	Variable 8
1	32.92601	31.68917	31.47486	34.07226	39.19825	45.79482	48.01601	47.0705
2	31.43586	28.39436	29.51405	35.74054	29.69695	40.35142	37.04941	40.44129
3	25.52328	30.29948	30.08692	32.02789	37.12829	33.05815	43.50836	43.33377
4	35.01418	32.0571	33.0491	30.18888	35.18198	45.053	42.63002	36.92911
5	35.20356	30.17122	41.65994	37.48748	41.03257	35.56017	37.79386	46.41008
6	34.21507	35.63817	34.38547	36.56249	32.52281	35.86547	48.30091	38.45383
7	28.77597	33.24676	33.85016	36.99472	33.34989	35.71104	49.27239	45.11844
8	35.92942	29.30705	42.9729	31.26369	38.21577	36.25551	43.98619	41.70616
9	33.22798	34.70188	31.85472	31.08599	37.00423	36.93539	40.28914	42.17984
10	35.38812	27.42618	31.32716	34.66871	41.95037	38.49905	35.51128	41.63984
11	30.21958	36.5177	34.22134	32.67303	35.81277	36.24145	40.98327	37.49252
12	31.27622	32.01239	38.37661	33.54002	34.20047	40.07304	45.30322	43.54768
13	31.48647	34.88103	28.34937	35.06172	39.26944	40.1278	41.35091	40.53129
14	33.92013	28.69174	34.91169	37.8405	38.56839	40.42313	38.67836	43.6566
15	29.66591	30.56473	37.55802	23.17105	30.34658	37.05556	46.18009	42.6303
16	31.10844	33.67103	38.29113	38.76417	35.46254	42.67893	42.27434	39.26209
17	40.02643	31.11984	27.58254	35.29507	41.11724	34.63456	39.15575	42.54477
18	32.39758	38.69437	33.76528	36.00588	43.67111	38.9823	37.19663	42.73088
19	32.09575	32.85204	35.92631	30.78779	36.53119	40.91484	43.87316	39.64461
20	37.88168	35.4559	34.65568	32.3288	37.79726	34.47026	39.82298	45.34026
21	34.59008	31.77265	37.46558	35.49285	38.3307	38.77921	37.43059	34.73544
22	28.92442	35.02926	37.72463	34.91202	32.10022	36.7457	45.81571	41.2374
23	33.68217	32.76095	33.57222	33.4424	28.25502	38.36216	35.39884	40.94948
24	30.33632	31.37054	30.69269	38.20444	37.72066	30.03953	39.27283	42.49215
25	30.8532	34.39439	40.8021	37.2953	36.89702	39.24234	41.55911	44.41334
26	30.3137	34.14751	39.04088	32.93347	43.97201	38.12175	43.2205	41.32036
27	31.98299	31.1571	33.17324	37.68959	37.43404	40.99423	36.46121	41.90423
28	31.9545	32.65845	39.7238	39.78145	32.3107	39.17859	34.0946	41.0604
29	32.85007	35.4217	32.17662	34.74896	40.03007	39.58759	40.86384	39.09449
30	30.93037	36.06698	31.00241	43.56337	38.99412	29.2117	43.29934	43.88565
31	35.73612	37.06123	30.75548	30.52981	37.99052	47.46524	36.57742	43.04262
32	32.59803	30.34646	36.25796	39.31325	35.62732	41.27641	39.45882	43.92968
33	31.15604	35.2129	29.85998	42.96103	37.90487	43.72088	35.89604	39.03072
34	35.06258	32.19548	34.54487	40.45457	38.14028	37.65143	39.6778	41.75673
35	31.69853	36.65835	32.80755	34.82718	34.75155	43.26499	38.89494	33.06273
36	32.25991	34.32994	35.60824	33.68746	43.05108	36.66553	39.00073	37.62138
37	35.4999	33.35635	35.66072	32.9988	37.26922	41.42929	41.03072	38.82927
38	27.92073	33.60703	34.07415	33.25954	41.36753	41.88643	52.48804	43.43399
39	28.31874	30.88468	32.64645	34.27681	38.65743	34.32129	40.60266	37.90604
40	29.15931	33.04723	36.83562	37.19231	34.63052	33.46872	42.74352	38.15287
41	26.18437	30.71678	35.52494	41.47684	42.66158	39.84002	44.8775	51.03219
42	28.13318	33.49362	37.26403	38.84442	33.73361	42.01188	40.58297	47.87718

43	27.43843	34.56678	32.46944	32.42024	31.91434	34.93233	36.18043	48.54508
44	38.41385	33.06527	29.43786	37.48314	30.85501	41.5662	43.06343	44.36423
45	27.60296	40.13448	36.65008	36.26474	46.86101	39.09495	37.86615	42.86081
46	29.87623	32.48961	36.14025	36.30738	41.53294	40.58606	41.87044	35.24006
47	31.79935	29.04783	39.68525	39.94501	33.85979	44.58763	33.19614	40.20092
48	31.78852	34.65131	33.65052	35.427	44.36366	36.54615	41.65836	31.22742
49	34.79348	34.432	36.48121	35.82733	45.16779	42.31196	45.9892	40.13347
50	29.57615	29.95434	34.07898	38.55097	37.5813	35.78051	35.18153	45.09232
51	33.709	35.30105	38.84506	38.29049	36.57534	32.31498	41.95027	47.65249
52	34.27901	36.8485	37.08557	34.34458	37.33769	40.21635	36.20836	41.4644
53	30.43774	37.96147	32.76437	42.76723	36.41297	37.24835	43.57484	39.55378
54	32.74894	37.38526	32.55049	34.13917	41.66416	44.28188	40.20264	45.55563
55	31.56733	40.62415	32.88478	39.00993	33.56897	41.05789	39.37754	46.85442
56	28.72093	31.25797	30.50324	39.44912	35.69942	41.77696	41.16888	38.05154
57	29.33364	29.68784	30.34201	36.65341	36.7317	36.10041	45.4417	40.69443
58	25.90265	35.80395	34.48435	31.87473	36.25283	39.90523	38.16464	43.24827
59	33.61281	39.37891	38.61483	29.22593	34.38479	34.97814	40.1136	47.24161
60	26.79713	28.90518	38.11155	35.7133	40.50008	39.32722	34.53573	40.85807
61	33.37088	36.32653	36.31754	38.03838	33.9606	37.12468	44.97935	34.19751
62	33.29862	31.00978	32.29301	33.63385	39.11077	37.71505	42.1913	46.61987
63	37.689	25.22878	34.29722	45.7739	41.99304	41.26367	42.41567	38.7641
64	31.00107	37.54633	37.90745	38.50459	40.74683	31.41509	42.84688	39.85934
65	36.26348	36.11699	36.76797	37.06662	36.74284	46.40698	38.27602	50.07242
66	36.59772	37.18658	35.24437	41.87215	39.52449	31.93284	29.92245	44.15195
67	29.39969	29.59146	39.41599	29.32688	38.46297	34.01586	36.91561	35.61667
68	37.31148	33.95917	34.73001	33.8886	40.39386	38.64935	44.20442	45.47714
69	32.32854	26.09238	35.31739	41.15104	42.9727	40.65734	47.01826	45.75723
70	32.16993	33.81683	38.79115	28.45428	38.76225	38.26008	38.74091	42.95688
71	35.62551	28.07731	35.13857	42.16839	37.06408	38.56276	44.11839	38.44145
72	27.10491	35.97183	31.03378	39.5981	35.30079	39.48431	47.34265	48.12316
73	32.68262	38.31062	33.11751	38.41123	36.27616	33.93453	37.66718	46.12684
74	29.98641	32.40585	31.7525	31.73508	33.00081	38.88774	38.42006	51.28173
75	33.09915	36.91635	35.98381	36.49485	34.97537	37.3288	47.67638	36.42657
76	27.80758	31.51446	40.17117	36.75788	38.34755	43.09933	38.07576	46.29861
77	33.99271	34.86757	29.21037	32.73438	34.85654	42.1473	41.28309	41.12227
78	35.99086	36.39049	42.12755	37.20694	35.40604	46.03292	44.66941	44.823
79	29.77213	38.42757	37.3388	40.17073	39.94571	39.76233	41.76121	39.99552
80	28.43039	29.92945	37.01119	37.67616	40.83359	40.81539	42.99317	49.3053
81	31.36784	34.07429	32.14832	32.13924	40.10178	45.24386	40.70527	42.27296
82	34.86155	32.27363	35.43569	36.1766	29.18782	35.2397	38.52755	54.83096
83	34.38821	27.89967	36.56111	40.36508	33.031	43.04049	42.06119	43.74193
84	33.79779	37.72698	33.38504	37.917	39.62658	44.15631	40.00294	42.36791
85	39.06082	32.33114	33.53446	35.26533	34.12077	37.42461	31.55331	49.05633
86	36.39594	32.9206	31.93394	39.19611	39.37449	33.75401	41.42041	42.04361
87	33.44156	35.09372	25.7681	35.62773	31.67167	39.62409	45.23882	39.4334
88	33.10049	27.0028	35.79919	35.14019	31.22167	42.56305	44.50536	36.53591
89	34.16331	29.17899	28.81033	39.06276	34.52206	32.85	42.51124	46.03127
90	30.60042	32.56253	31.20073	36.84747	36.14064	36.41787	34.71745	40.31396

91	32.49754	33.41312	31.64427	33.11962	42.21118	42.83778	43.70442	44.94825
92	22.15886	30.66583	27.21521	34.4425	39.76029	43.40977	37.26835	44.53675
93	30.72273	31.90988	33.27271	36.3918	35.91251	43.9091	46.44364	44.67753
94	37.01734	31.62779	34.9575	29.78731	40.30314	38.08922	49.8278	49.55136
95	30.65545	41.18574	34.79465	40.88882	32.7685	41.64187	40.46224	37.21432
96	30.12558	35.72305	40.36197	35.91972	35.04119	49.1124	33.42748	45.81633
97	36.87369	34.19729	35.05101	34.5747	36.00502	35.3282	39.87626	36.1637
98	32.99889	39.17385	33.92429	40.81654	38.86608	38.00475	46.75181	48.39247
99	29.04389	33.18395	36.10558	31.50654	37.55102	37.55409	39.58435	47.42128
100	34.50125	33.89293	37.87164	33.9439	33.32836	37.80936	44.33889	44.09404

Run	Variable 9	Variable 10	Variable 11	Variable 12	Variable 13	Variable 14	Variable 15
1	46.42641	42.71915	43.42528	43.3253	44.44667	42.18537	45.66628
2	41.32131	37.47078	49.10537	38.40539	45.72312	42.69364	49.12879
3	44.32303	45.00476	42.33161	47.16806	47.65289	36.03509	44.97308
4	39.61775	52.62077	42.56509	51.61833	44.54323	43.10763	37.2193
5	40.19843	33.77708	50.02575	41.44258	46.45288	45.94126	42.50953
6	44.8154	47.92178	44.00134	48.78041	47.89841	42.06767	39.80517
7	42.36039	47.23037	40.33788	42.98817	42.06494	46.92589	40.53362
8	40.35186	42.85277	39.89051	52.42157	38.99105	45.37183	41.67521
9	41.61009	43.63606	51.02235	41.1824	42.6465	48.89857	32.80774
10	45.62095	48.32301	49.04111	52.06203	42.00512	43.28498	38.43643
11	39.21347	42.98648	51.63962	46.1359	39.60286	46.43121	48.00097
12	49.53641	40.60345	43.80398	39.67779	44.68232	41.36705	37.94745
13	41.21119	39.15215	39.63049	45.77522	36.92258	34.89698	36.59387
14	48.00003	47.97047	41.03069	48.45898	43.0341	39.32153	47.66898
15	46.73441	43.40283	45.68897	46.23576	37.65972	42.32895	44.71712
16	37.87106	46.79076	41.60885	40.77886	49.58017	41.9193	39.93293
17	44.91455	46.85625	45.45854	44.97714	44.89365	51.53663	39.11918
18	46.28012	53.61092	49.3046	43.50488	39.87749	40.25907	40.8167
19	43.84303	39.89987	44.74496	41.99857	47.21757	42.49043	34.24629
20	49.32212	43.29468	50.93401	43.95885	33.84012	40.68095	43.19258
21	44.73682	49.97461	43.62357	36.7909	53.05498	47.75636	49.81177
22	41.1106	45.59137	39.04957	40.79329	41.14997	43.62412	42.05645
23	46.16122	53.8882	52.60858	51.22205	45.26137	43.50979	43.47512
24	48.60369	50.53735	48.50161	43.85756	43.74375	40.52766	38.62675
25	45.14567	43.72988	38.49486	47.27347	47.03223	49.23184	46.58131
26	50.50009	48.08213	42.99924	38.01414	42.67004	40.18036	40.73446
27	47.27995	49.19558	44.35209	38.99179	47.34624	39.21333	46.46391
28	44.46978	41.87425	49.81842	48.69979	43.95556	38.50769	37.34135
29	45.06058	43.80915	43.48099	47.74947	44.28341	44.45551	42.33978
30	51.96302	40.13582	42.24858	49.99582	48.99309	42.85027	38.46744
31	46.56021	44.29885	47.32433	33.35557	41.34561	40.4563	46.21512
32	42.28747	41.2192	52.09398	45.69835	43.47579	42.42262	39.59546
33	43.65709	48.8977	37.19361	45.51175	38.01242	43.8123	45.57839
34	44.37405	44.82506	47.43601	44.04819	37.31522	38.19015	37.77824
35	38.38641	50.29841	46.32465	53.30142	47.54893	42.98378	40.26731
36	45.92678	39.49319	44.17962	45.19541	54.88191	39.82222	41.93731
37	44.1801	46.39373	43.87433	42.42575	47.96606	48.23128	44.19759
38	54.99181	46.5594	40.48813	44.7963	42.38543	44.85828	35.08066
39	46.01608	46.08931	46.73752	44.25261	45.12607	44.04988	39.759
40	43.15816	41.32933	47.90425	42.97452	42.49459	48.46893	42.44851
41	43.47476	43.95829	53.27538	43.23686	52.84083	39.83334	45.24571
42	46.83881	45.70981	43.2397	54.55051	41.79499	44.68961	38.2665
43	47.45511	47.68984	41.29008	44.5826	48.57932	37.85667	44.48406
44	43.0994	41.69495	44.64027	49.15138	49.38996	48.72662	48.37793
45	40.82883	44.1579	41.69128	47.57984	42.26625	41.00905	39.45131
46	50.97343	42.49479	52.86529	48.18907	35.74519	43.88856	46.86119

47	45.72155	46.68349	50.27735	46.63321	48.17977	37.04071	39.34518
48	43.39719	51.027	46.57998	49.30574	46.54589	35.5817	50.17176
49	39.28539	41.50365	50.06796	41.53929	44.2033	50.52735	43.41712
50	44.58207	43.52915	36.13942	44.40639	45.03786	43.70958	43.60632
51	41.78818	47.56374	38.06111	44.87271	43.20728	38.72618	47.7425
52	51.25635	42.28537	43.04431	49.58878	46.87477	46.23825	42.23003
53	45.51426	45.5052	46.46744	47.40337	36.52745	44.13546	51.47539
54	43.73335	38.89286	41.90851	43.70126	46.83183	39.9986	43.93976
55	36.57667	38.34622	44.51696	47.84484	53.87427	33.38586	42.87312
56	46.60229	37.04678	48.64318	50.48369	50.64972	46.1341	45.23208
57	40.5975	51.95824	46.8912	50.16471	41.6857	45.70636	44.02983
58	48.09121	40.82912	48.70303	41.68924	39.44658	41.50437	34.6504
59	42.69128	56.52433	58.40272	43.45451	47.47496	35.1717	41.13759
60	48.25525	49.07424	45.23749	42.16579	46.3315	52.05499	47.03003
61	45.43375	35.60179	51.69682	45.99934	48.89235	36.72194	41.20842
62	43.32645	40.99109	52.39876	49.69625	46.14498	39.04446	30.98692
63	42.94041	42.03385	46.19267	45.0803	39.086	38.70817	45.37829
64	42.07405	47.39848	44.33304	46.35446	52.19895	47.28964	41.39009
65	48.82905	49.7286	42.83132	52.86482	38.32977	46.61831	41.06526
66	50.0035	44.12591	30.71686	42.81579	45.576	50.59157	38.99898
67	42.46794	43.17311	46.39356	47.1057	44.07979	39.45803	43.11454
68	38.76712	42.20219	48.14936	51.06317	43.85731	44.65443	44.75032
69	39.81387	51.38747	45.37569	38.64209	38.70106	47.27416	43.73246
70	34.96264	45.19703	42.00651	53.6093	41.60622	41.33353	50.67126
71	41.91277	51.99026	44.87313	47.91163	49.2161	40.93415	36.92962
72	42.59907	55.28253	47.27458	44.12636	35.04382	45.85441	42.94623
73	38.92895	48.69961	45.55386	42.65866	51.5948	47.0924	41.79879
74	39.98946	49.55358	49.64492	39.14962	42.95709	49.5714	35.75459
75	50.43818	48.46679	50.61685	44.56712	48.40124	43.14421	43.81856
76	38.12428	46.9732	45.08684	46.65962	40.5991	32.97828	43.32747
77	47.69096	37.96473	40.78487	35.8425	40.81689	41.66533	45.92781
78	48.52499	45.90821	48.20851	45.27788	45.37902	39.58944	37.64041
79	41.45036	44.41478	48.86924	41.8339	39.99385	40.76766	42.72754
80	42.86462	40.68428	50.50903	55.2187	43.62478	46.66095	42.13371
81	35.82587	50.12588	40.9961	57.77116	45.81318	45.21976	35.96487
82	47.01823	45.77909	47.53002	40.16424	45.50173	45.00351	41.64098
83	44.06863	49.28104	39.46191	39.64509	44.82642	36.44072	38.86767
84	53.82868	45.18019	51.30925	46.77949	48.55388	47.52588	40.9226
85	37.58927	36.64498	37.60517	46.48131	40.20992	45.05734	42.66704
86	40.63329	53.1863	53.68127	41.15702	40.46148	37.37848	41.51297
87	52.47833	47.07865	45.94169	50.78646	43.5784	37.66866	46.30382
88	47.204	44.93117	47.87578	45.89681	43.36329	53.83749	36.38983
89	49.80785	39.55103	48.35888	49.39419	40.31854	41.82999	48.75793
90	39.63481	44.53698	47.07329	46.9516	45.91077	43.34105	40.44855
91	42.01614	46.23533	55.451	40.47992	51.39919	44.32365	44.28186
92	37.28552	42.64253	46.9934	45.4194	49.96136	42.65113	40.3508
93	43.95775	51.12512	44.95939	37.05983	50.81277	41.68665	44.54
94	45.33849	47.54474	42.7401	48.08673	50.22354	38.13105	47.31971

95	33.67846	40.31369	46.10691	39.9547	42.82353	47.9586	45.07177
96	47.78493	50.70316	54.7947	51.55876	40.95568	45.62646	53.05642
97	35.56921	48.53209	45.82181	42.47114	41.48447	41.19878	45.88499
98	40.99245	45.37179	54.26757	48.29765	46.0414	45.48679	40.11326
99	48.98077	46.20874	49.54985	48.92655	49.86784	49.94249	47.2344
100	36.82265	44.72216	47.67506	50.23312	46.62376	44.21215	49.00813

NO. OF COPIES ORGANIZATION

1 (PDF ONLY) DEFENSE TECHNICAL INFORMATION CTR
DTIC OCA
8725 JOHN J KINGMAN RD
STE 0944
FORT BELVOIR VA 22060-6218

1 US ARMY RSRCH DEV & ENGRG CMD
SYSTEMS OF SYSTEMS INTEGRATION
AMSRD SS T
6000 6TH ST STE 100
FORT BELVOIR VA 22060-5608

1 DIRECTOR
US ARMY RESEARCH LAB
IMNE ALC IMS
2800 POWDER MILL RD
ADELPHI MD 20783-1197

1 DIRECTOR
US ARMY RESEARCH LAB
AMSRD ARL CI OK TL
2800 POWDER MILL RD
ADELPHI MD 20783-1197

1 DIRECTOR
US ARMY RESEARCH LAB
AMSRD ARL CI OK T
2800 POWDER MILL RD
ADELPHI MD 20783-1197

1 AEROPREDICTION INC
ATTN F MOORE
9449 GROVER DRIVE STE 201
KING GEORGE VA 22485

1 UNIV OF TEXAS AT ARLINGTON
MECH & AEROSPACE ENG DEPT
ATTN J C DUTTON
BOX 19018
500 W FIRST ST
ARLINGTON TX 76019-0018

2 ATK TACTICAL SYSTEMS DIV
ALLEGANY BALLISTICS LAB
ATTN D J LEWIS J S OWENS
210 STATE ROUTE 956
ROCKET CENTER WV 26726

1 ATK ADVANCED WEAPONS DIV
ATTN R H DOHRN
MN06-1000
4600 NATHAN LANE N
PLYMOUTH MN 55442

NO. OF COPIES ORGANIZATION

1 ATK ORDNANCE SYS
ATTN B BECKER
MN07 MW44
4700 NATHAN LANE N
PLYMOUTH MN 55442

1 SCIENCE APPLICATIONS INTL CORP
ATTN J NORTHRUP
SUITE 1610
8500 NORMANDALE LAKE BLVD
BLOOMINGTON MN 55437

3 GOODRICH ACTUATION SYSTEMS
ATTN T KELLY P FRANZ
J CHRISTIANA
100 PANTON ROAD
VERGENNES VT 05491

3 ARROW TECH ASSOC
ATTN W HATHAWAY J WHYTE
MARK STEINOFF
1233 SHELBURNE RD STE D8
SOUTH BURLINGTON VT 05403

1 KLINE ENGINEERING CO INC
ATTN R W KLINE
27 FREDON GREENDEL RD
NEWTON NJ 07860-5213

1 GEORGIA INST TECH
DEPT AEROSPACE ENGR
ATTN M COSTELLO
270 FERST STREET
ATLANTA GA 30332

1 AIR FORCE RSRCH LAB
AFRL/MNAV
ATTN G ABATE
101 W EGLIN BLVD STE 333
EGLIN AFB FL 32542-6810

1 COMMANDER
US ARMY ARDEC
ATTN AMSRD AAR AEM A G MALEJKO
BLDG 95
PICATINNY ARSENAL NJ 07806-5000

1 COMMANDER
US ARMY ARDEC
ATTN ASMRD AAR AEP E D CARLUCCI
BLDG 94
PICATINNY ARSENAL NJ 07806-5000

NO. OF
COPIES ORGANIZATION

1 COMMANDER
US ARMY ARDEC
ATTN ASMRD AAR AEP E C KESSLER
BLDG 3022
PICATINNY ARSENAL NJ 07806-5000

1 COMMANDER
US ARMY ARDEC
ATTN ASMRD AAR AEP E
I MEHMEDAGIC
BLDG 94
PICATINNY ARSENAL NJ 07806-5000

1 PRODUCT MGR SMALL AND MED
CALIBER AMMO
ATTN SFAE AMO MAS SMC R KOWALSKI
BLDG 354
PICATINNY ARSENAL NJ 07806

1 PM MAS
ATTN SFAE AMO MAS
BLDG 354
PICATINNY ARSENAL NJ 07806-5000

3 US ARMY AMRDEC
ATTN AMSAM RD SS AT L AUMAN
R W KRETZSHMAR E VAUGHN
REDSTONE ARSENAL AL 35898-5000

1 COMMANDER
US ARMY ARDEC
ATTN AMSTA DSA SA A CLINE
BLDG 151
PICATINNY ARSENAL NJ 07806-5000

1 ATK ORDNANCE SYSTEMS
ATTN B BECKER
MN07-MW44
4700 NATHAN LANE NORTH
PLYMOUTH MN 55442-2512

ABERDEEN PROVING GROUND

1 DIRECTOR
US ARMY RSCH LABORATORY
ATTN AMSRD ARL CI OK (TECH LIB)
BLDG 4600

NO. OF
COPIES ORGANIZATION

12 DIRECTOR
US ARMY RSCH LABORATORY
ATTN AMSRD ARL WM J SMITH
AMSRD ARL WM B M ZOLTOSKI
AMSRD ARL WM BC P PLOSTINS
J NEWILL M CHEN (3 CYS)
J DESPIRITO J SAHU
B GUIDOS S SILTON
P WEINACHT